Saudi Journal of Biological Sciences 28 (2021) 5971–5985

Contents lists available at ScienceDirect

Saudi Journal of Biological Sciences

journal homepage: www.sciencedirect.com

Original article

Prospective of biosynthesized *L.satiVum* oil/PEG/Ag-MgO bionanocomposite film for its antibacterial and anticancer potential

M. Amina [a,*], N.M. Al Musayeib [a], G.A. Al-Hamoud [a], A. Al-Dbass [b], A. El-Ansary [c], M.A. Ali [d]

[a] Department of Pharmacognosy, Pharmacy College, King Saud University, Riyadh 11451, Saudi Arabia
[b] Biochemistry Department, College of Sciences, King Saud University, Riyadh, Saudi Arabia
[c] Central Laboratory, Female Centre for Scientific and Medical Studies, King Saud University, Riyadh, Saudi Arabia
[d] Department of Botany and Microbiology, College of Science, King Saud University, Riyadh 11451, Saudi Arabia

ARTICLE INFO

Article history:
Received 19 May 2021
Revised 19 June 2021
Accepted 20 June 2021
Available online 24 June 2021

Keywords:
Lepidium sativum
Essential oil
Polyethylene glycol
Bionanocomposites
Antiacterial
Anticancer

ABSTRACT

A substantial interest has been manifested in utilizing oil/metal oxide hybrid bionanocomposite, especially organic/ inorganic to design different biomedical applications. The present study reports the synthesis, characterization, antibacterial and anticancer properties of biogenic silver nanoparticles (AgNPs) and *L.satiVum* oil/PEG/Ag-MgO bionanocomposite. The fabricated AgNPs and *L.sativum* oil/PEG/Ag-MgO bionanocomposite were characterized by employing different spectroscopic (UV, FTIR, XRD) and microscopic (TEM, SEM) techniques. The particle size analysis showed that the mean size of 16.32 nm for AgNPS and 13.45 nm *L.satiVum* oil/PEG/Ag-MgO, indicating the excellent dispersion of Ag-MgO nanoparticles in the PEG– *L.satiVum* oil matrix. The antimicrobial activity of AgNPs and polymeric bionanocomposite was investigated against two pathogenic bacteria. The highest antibacterial effect was observed for bionanocomposite towards Gram-positive *Staphylococcus aureus* (27 mm) and Gram-negative *Escherichia coli* (25 mm) at 40 μg/well. The bionanocomposite completely vanished the bacterial growth (100%) at 80 μgmL^{-1} concentrations. Moreover, the AgNPs and polymeric bionanocomposite was evaluated for anticancer activity against human cervical cancer cells (HeLa cells) at different doses (50, 250, 500, and 1000 μgmL^{-1}). The results showed polymeric bionanocomposite was stronger in inducing the HeLa cancer cell death than AgNPs. Overall, the fabricated *L.satiVum* oil/PEG/Ag-MgO bionanocomposite serve as a potential antimicrobial and anticancer agent and could be used in the development of novel drugs and health care products in near future.

1. Introduction

Bionanocomposites have emerged as an advanced group of nano-sized materials obtained from the combination of biopolymers such as polysaccharides, nucleic acid, proteins, and essential oils with inorganic solids at nanometric scale (Mousa et al., 2016). They possess the synergism between the exceptional features of inorganic fillers (excellent mechanical strength, high thermal stability, optical behavior, etc.) with those of the biopolymeric matrix (biodegradability, biocompatibility, etc.). The resultant bionanocomposites exhibit improved thermal, optical, mechanical, magnetic, photoelectronic and biological properties (Zia et al., 2020). These biohybrid finds application in various fields including; food packaging (Zubair and Ullah, 2020), biomedical materials (Ismail and Razali (2020)), drug delivery systems (Patwekar, 2016), agriculture sector (Zhang et al., 2020), sensing and electronic materials (Burrs et al., 2015; Liu et al., 2019).

Recently, the functionalizations of renewable resources-derived polymers via incorporation of metallic nanoparticles have become an area of huge interest, where innate features of nanoparticles are bestowed into the polymer matrix (Hanisch et al., 2011). The resultant environmental benign bionanocomposite combines both the characteristics, superiority of low-dimensional organic layers and wide surface area of nanoparticles, thus creating a broad spectrum of applications in manufacturing and science (George et al., 2018). These bionanocomposites are multifaceted, significantly biodegradable, and their polymer can be obtained from the vast diversity of sustainable precursors, including oxygen-rich and

* Corresponding author.
E-mail address: mamina@ksu.edu.sa (M. Amina).
Peer review under responsibility of King Saud University.

Production and hosting by Elsevier

https://doi.org/10.1016/j.sjbs.2021.06.052
1319-562X/

hydrocarbon-rich monomers (Mhd Haniffa et al., 2016). The most commonly used sustainable bioresources are edible and non-edible oils. The plant oils appear to be the best suitable preliminary component for the production of polymeric bionanocomposite as they are ample, biodegradable, environment friendly, and economical (Ribeiro-Santos et al., 2017). Various vegetable oils including; olive, soybean, rapeseed, linseed, cottonseed, castor, Jojoba and rubber seed oil are being used by chemical industries for the manufacture of coatings, lubricants, paints, surfactants, soaps and cosmetic products from decades (Alam et al., 2014; Samarth and Mahanwar, 2015).

L. sativum seed oil (LSO) is one of the important oil and widely found across the world. It is comprised of balanced amounts of polyunsaturated fatty acids (46.8%) and monounsaturated fatty acid (37.6%). LSO is relatively stable oil owing to its high content of natural antioxidant components such as tocopherols carotenoids and phytosterols (Diwakar et al., 2010). The oil has been reported to possess various biological activities including, antimicrobial, antioxidant, anticancer (Alqahtani et al., 2019), analgesic, anti-inflammatory, antiulcer, antipyretic (Al-Yahya et al., 1994), antihypertensive (Maghrani et al., 2005), diuretic (Patel et al., 2009), nephroprotective (Yadav, 2010), antiasthmatic (Paranjape and Mehta, 2006), hepatoprotective and hypoglycemic (Abuelgasim et al., 2008) properties. The oil has also shown synergistic effects by inhibiting the levels of thromboxane B2 and platelet aggregation in lung and spleen tissues in Wistar rats (Raghavendra and Akhilender Naidu, 2011). Recently, an oil-based polymeric material has grabbed immense attention and extensive research work is being carried out to manufacture these biopolymeric materials owing better chemical and physical properties (Imre and Pukánszky, 2013). Several biodegradiable polymers such as polyurethane, polyesteramide, polyetheramide, alkyd, epoxy, polystyrene and polyvinyl alcohol have been used to prepare these oil-based biopolymers (Song et al., 2018; De Conto et al., 2020). The oil-based polymeric materials or coatings have shown a vast range of desired potential such as biocompatibility (Arevalo et al., 2018), moderate hydrophilicity (Bai et al., 2017), optical transparency (Ahmad et al., 2014), biomaterials (as antimicrobial surfaces and biocompatible) (Matharu et al., 2018), pharmaceutical industry (as coatings for medicine) (Vasile, 2018) and electronics (as superior layers in organic and hybrid devices) (Bazaka et al., 2011). Among various polymers, polyethylene glycol (PEG) is the most biocompatible hydrophilic polyether, synthetic polymer that has shown many biomedical and chemical applications due to its non-toxic and high solubility nature. It is used in various pharmaceutical ointments, creams, binding and dispersing agent, coatings in various scenarios and medical solvents. PEG has been reported to serve as bioconjugate to various illness drugs by coupling itself with the target drug to improve the pharmacokinetic features of drug treatment (Hoang Thi et al., 2020).

The introduction of inorganic particles onto the surface of polymer matrix may further improve the properties oil-based polymeric film. Nanoparticles dimension less than 100 nm are considered as idle substances to strengthen the polymer matrix without interfering the transparency and other features of the film (Gupta and Tomoko, 2020). Among various metals, magnesium oxide (MgO) is the most promising functional metal oxides candidate due to its excellent and unique optical, thermal, high ionic character, electrical, chemical and mechanical properties (De Silva et al., 2017). MgO finds various applications including high-temperature insulating materials in fuel–oil additives, catalyst, heat-resistant, superconducting materials, synthesis of refractory ceramics, an adsorbent for removing heavy metals and dyes from wastewater toxic and waste remediation (Hornak et al. 2018). Magnesium oxide nanoparticles (MgONPs) are basic interesting oxide that has remarkable surface reactivity, biocompatible with high concentration of corner sites, highly stable under extreme conditions, less toxic and can be synthesized from economical precursors (Khalid et al., 2019). These nanoparticles exhibited enhanced biomedical potential, including; antimicrobial (Nguyen et al., 2018), antioxidant (Sushma et al., 2016), anticancer (Behzadi et al., 2019), anti-inflammatory (Climent et al., 2007), analgesic (Torabi et al., 2018), anti-diabetic (Moeini-Nodeh et al., 2017) and bone regeneration (Hickey et al., 2015). MgONPs has been acknowledged by the US Food and Drug Administration as non-toxic and environment friendly in nature that can be readily used in pharmaceutical industry (Cai et al., 2018). However, the aforementioned applications are largely due to the controlled size, morphology and structure because of its variations in chemical and physical properties. Hence, to prepare MgO nanomaterials with diverse competence, it is necessary to modify size, morphology and surface chemistry as the above-stated applications arise on the surface of nanoparticles (Jayapriya et al., 2018). Thus, the fabrication of nanomaterials with different morphologies provides reaction specificity due to the formation of different surface atoms and crystallographic facets. In recent times, various reports on MgO-metal based nanomaterials are documented in the literature which is actively being used for multiple purposes (Liong et al., 2008). Several studies have shown that metal/metal oxide expressed better antibacterial effects towards many Gram-positive and Gram-negative bacteria (Abudula et al., 2020). Thus, the present study aims to develop oil based polymeric Ag/MgO bionanocomposite to improve the surface morphology of polymeric bionanocomposite for the up-gradation of its biological and physio-chemical potential. Silver nanoparticle (AgNPs) is well known for their extensive scope of antimicrobial, anticancer, antioxidant, anti-inflammatory and catalytic activities (Jayapriya et al., 2019; Gomathi et al., 2020; Reddy et al., 2015). AgNPs has expressed fascinating biological properties and at very low dose it is lethal to pathogens, but safe to human beings (Reddy et al., 2015). Several approaches have been applied to prepare metal/metal oxide nonanocomposites with different morphologies such as bimetallic alloys (Navya et al., 2019), core-shells (Chiozzi and Rossi, 2020), nanosheets (Pazmiño-Durán et al., 2001), nanorattle (Wu et al., 2011), nanotubes (Tripathi et al., 2017) and yolk-shell (Moon, 2020) etc. The fabrication of these nanostructures involves various physiochemical procedures that have been generated hazardous byproducts, rigorous energy and harsh environmental conditions. Consequently, there is an increase demand for the development of a lucrative, environmentally friendly approach that gives a superior platform to synthesize the Ag/MgO bionanocomposite with a well-defined morphology that can serve as a potential candidate to resolve varied problems with multifunctional properties (Jayapriya et al., 2020; Ayinde et al., 2018).

Considering the unique individual properties of *L. sativum* seed oil, PEG and Ag/MgONPs, we herein report the fabrication and characterization of of *L. sativum* oil/PEG bionanocomposite decorated with Ag/MgO nanoparticles. The pre-synthesised bionanocomposite was tested for antibacterial and anticancer potential. To the best our knowledge, this is the first study on the synergy between *L. sativum* oil and Ag/MgONPs in an eco-friendly coating context.

2. Materials and methods

2.1. Chemicals and reagents

Ethanol (96%), Petroleum ether (40–60 °C), Dimethyl sulfoxide (DMSO, ≥99.9%) Silver nitrate (AgNO3, ACS reagent, ≥99%), Polyethylene glycol-2000 (PEG-2000), Magnesium nitrate hexahydrate (Mg(NO3)2·•6H2O, ≥98%) 2.5% glutaraldehde, Paraformaldehyde,

Anhydrous sodium sulfate (Na2SO4, ≥99%), Anhydrous sodium hydroxide (NaOH, ≥98.0%), 3-(4, 5- dimethylthiazol-2-yl)-2,5-dip henyltetrazole bromide (MTT), Dulbecco's Modified Eagle's Medium (DMEM), Fetal bovine serum (FBS), Antibiotic antimycotic solution, phosphate buffer solution (PBS, pH 7.4), Ethylenediaminetetraacetic acid (EDTA), β-Nicotinamide adenine dinucleotide (NADH), Sodium pyruvate (≥99%), Proteinase K, Ethidium bromide solution, Agarose gel, were acquired from Sigma-Aldrich. The Nutrient agar broth was supplied by HiMedia.

2.2. Botanical sample and oil extraction

The seeds of *L. sativum* were purchased from a local supermarket of Riyadh, Saudi Arabia and taxonomically identified by Prof. Dr. Mohamed Yousef, at College of Pharmacy, King Saud University. The seeds were screened manually and the best ones were chosen. The collected seeds were dried, powered in an electric grinder and oil was extracted with petroleum ether for 24 h in a Soxhlet apparatus as per method described earlier (Khan et al., 2016). The oil was freed from petroleum ether by evaporation on rotary at ± 25 °C under reduced pressure. To determine the total oil content, 12.0 g triplicates of powdered seeds were extracted in a Soxhlet apparatus for 24 h. After the removal of petroleum ether the weights of residual oil were calculated. The obtained oil was dried over anhydrous sodium sulfate, transferred in capped glass vials and stored in refrigerator at 4 °C.

2.3. Analysis of L. Sativum oil

Chemical composition analyses of the essential oils of *L. sativum* was conducted on GC–MS/FID (QP2010 Ultra, Shimadzu Corporation, Kyoto, Japan), equipped with an AOC-20i Autosampler (Shimadzu). Rtx®-5MS Restek fused silica capillary column (5%-diphenyl–95%-dimethyl polysiloxane, 30 m × 0.25 mm i.d., film thickness 0.25 μm) was used for the separations of components. Helium (99.999%) was applied as the carrier gas at a constant flow rate of 0.7 mL/min. A 0.5 μL of injection volume with a split ratio of 1:10 was employed. The GC oven temperature was programmed as follows: start from 50 °C (isothermal for 10 min), then rising with 4 °C/min up to 210 °C, followed by an increase up to 250 °C at 5 °C/min rate.

A detector splitting system with split flow ratio 1:4 (MS:FID) was employed to acquire the simultaneous MS and FID data. Two restrictor tubes with 0.62 m × 0.15 mm i.d and 0.74 m × 0.22 m m i.d. dimensions were used to connect the splitter to the MS and FID detector, respectively. The MS data were obtained in the full scan mode (m/z of 40–350) at a 0.3 scan/s scan rate, using the electron ionization (EI) with 70 eV electron energy. The injector and ion-source and FID temperatures were maintained at 250 °C. Hydrogen, helium and air at a flow rate of 30, 30 and 300 mL/min, respectively, served as a gas supply for the FID. Each component was quantified by the normalization percentage of the peak area. The concentrations of each component were calculated from the GC peak areas without the correction factor and were arranged in the order of GC elution. The retention index and retention times were obtained by injecting a linear hydrocarbon mixture (C_7-C_{30}) under similar conditions. The components of oil were identified by comparing retention times, retention indexes and the mass spectra with those already reported in literature (Adams, 2007) and computerized matching of the acquired mass spectra with those stored in the NBS 54 K, NIST107, NIST21, and WILEY 8 mass spectral libraries of the GC–MS data system (Linstrom and Mallard, 2001).

2.4. Synthesis of silver nanoparticles using L. Sativum seed extract

The aqueous extract of *L. sativum* seed was prepared by taking 1:10 (w/v) proportion of a finely powdered seeds and double distilled H_2O. The aforementioned mixture was boiled under reflux conditions at for 30 min at 60 °C. Then, the extract was decanted and filtered using Whatman No. 1 filter paper to separate the suspended solid particles. The obtained filtrate was stored at 4 °C and used as a reducing and capping mediator for the fabrication of nanocomposite. 60 mL of the filtrate of the *L. sativum* seed was added to 90 mL of 1 mM silver nitrate ($AgNO_3$) in 250 mL conical flasks at the ratio of 2: 3 v/v for the reduction of Ag^+ to Ag°. The reaction mixture was then placed on a turntable domestic microwave oven and subjected to irradiation for different time intervals of 20, 40, 60, 80, and 100 s at a power of 700 W and frequency of 2450 MHz to complete bio-reduction. The preparation of silver nanoparticles (AgNPs) was monitored using UV–Vis Spectrophotometer over the wavelength range of 220–600 nm. Time-resolved absorption spectra of the UV–Vis spectroscopy were used in monitoring the periodic bioprocess growth kinetics of AgNPs through color variation. The prepared nanoparticle was used in subsequent experiments.

2.5. Synthesis of L. Sativum oil/PEG/Ag-MgO bionanocomposite

The *L. sativum* oil/PEG/Ag-MgO bionanocomposite was prepared through a"one-pot" process in *L. sativum* oil solution. Around 20 mL of the *L. sativum* oil and 10 g of polyethylene glycol-2000 (PEG 2000) was dissolved in 100 mL of ethanol and 100 mL of distilled water separately with continuous stirring at room temperature. Equal volumes of *L. sativum* oil (50 mL) and PEG-2000 (50 mL) were thoroughly mixed. After complete dissolution, 20 mL of 0.1 M magnesium nitrate hexahydrate ($Mg(NO_3)_2{\cdot}6H_2O$) with 2 mL of 0.1 M. NaOH solution was added drop wise to react with *L. sativum* oil/PEG solution in an aqueous bath system at 80 °C under gentle stirring. Stirring was continued for 2 h until a complete precipitation was achieved. After reaction was performed and the cream solid product was appeared, an aqueous mixture of *L. Sativum* seed: 1 mm AgNO3 (2:3 v/v%) was added into the above mentioned suspension, and the reaction mixture was subjected to controlled ultrasonic irradiation at100% amplitude (0.5 cycles) for 30 min. The product obtained was centrifuged for 10 min at 2500 rpm, filtered, and washed with ethanol to remove extra *L. sativum* oil and finally freeze dried.

2.6. Characterization of silver nanoparticles and L. Sativum oil/PEG/Ag-MgO bionanocomposite

AgNPs and *L. sativum* oil/PEG/Ag-MgO bionanocomposite have been characterized by using spectroscopic techniques such as ultraviolet–visible (UV–vis), Fourier transform infrared (FTIR), and X-ray diffraction (XRD). UV–vis spectra of green synthesized AgNPs and Ag-MgO/*L. sativum* oil bionanocomposite have been carried out on Ultrospec 2100-Biochrom spectrophotometer, (Biochrom Ltd, Cambium, Cambridge, UK). FT-IR of the pre-synthesized nanoparticles and bionanocomposite spectra have been recorded on a PerkinElmer FT-IR spectrophotometer (PerkinElmer Ltd, Yokohama, Japan). XRD measurements of biosynthesized samples were performed on EMPREAN PAN analytical diffractometer (Malvern Panalytical B.V., Eindhoven, Netherlands) employed with a Cu-Kα (λ = 1.5406 Å) radiation source. The morphology and size of AgNPs and bionanocomposites were studied using scanning electron microscopy (SEM, JSM-6390LV, JOEL Ltd, USA) and transmission electron microscope (TEM, JEM-3100F, JEOL Ltd, USA). Energy-dispersive X-ray spectroscopy (EDX, RONTEC's EDX system, Model

QuanTax 200, Germany) was performed to evaluate the components of the biosynthesized samples.

2.7. Antibacterial activity

2.7.1. Bacterial cell viability in the presence of L. Sativum oil/PEG/Ag-MgO bionanocomposite

The biosynthesized AgNPs and *L. sativum* oil/PEG/Ag-MgO bionanocomposite were tested for the bactericidal effect against *Staphylococcus aureus* (ATCC 25923) and *Escherichia coli* (ATCC 25922). Both the bacteria *S. aureus* and *E. coli* were procured from the Microbiology department of the King Khalid hospital (KKH) Riyadh, Saudi Arabia. The pure bacterial cultures were sub-cultured on nutrient agar broth under the optimum conditions with overnight shaking in an incubator. The growth of bacteria was determined by the turbidity of culture as a qualitative measurement and further confirmed by culture plate testing to measure the viability in the presence and absence of test samples. The rate of bacterial growth was determined by adding different concentrations (5, 10, 20, 40, 80 and 160 μgmL^{-1}) of the test sample to the liquid medium and incubated with the bacteria at 37 °C. Bacterial cultures without test samples were incubated in the similar medium under optimum growth conditions were chosen as control. Whereas, same concentrations of test sample without the bacteria in separate media were applied as blank controls to account for the optical interference by the light-scattering effects of the test sample. 1 mL of overnight incubated bacterial culture was served to inoculate the 100 mL of secondary culture (nutrient broth) with different doses of the test sample. The bacterial culture was incubated at 37 °C and the optical density was recorded every hour using UV–vis spectrophotometer (Evolution 20, Thermo Fisher Scientific). 0.1 mL of culture was taken from each treated flask and poured over the surface of media and incubated at 37 °C for 12 h. The number of colonies that appeared on the surface of the media was counted as an indicator of the number of bacteria. The result obtained was used to calculate the minimum inhibitory concentration and maximum bactericidal concentration of applied bionanocomposite.

2.7.2. Determination of antibacterial potential of AgNPs and bionanocomposite by zone inhibition assay

The antibacterial effects of the biosynthesized bionanocomposite against *S. aureus* and *E. coli* were tested. A fresh culture of both the microorganisms was sub-cultured in nutrient broth in conical flask and incubated for 12 h at 35 °C on an orbital shaker at 120 rpm. Also nutrient agar plates were prepared separately and inoculated with 100 mL of fresh culture of each bacterium (*S. aureus* and *E. coli*) by the spread plate procedure. A sterilized steel borer was used to prepare 8 mm well on these inoculated plates and molten agar was applied to seal the each well base to prevent the surface leakage of material. Each plate well was then filled with 100 mg of pre-synthesised bionanocomposite suspension and incubated for 12 h at 35 °C. After overnight incubation, the zone formation was noticed around the loaded material.

2.7.3. Effect of bionanocomposite on bacterial cell morphology

The cellular morphological changes of both the bacterial strains were examined by SEM before and after the treatment with different concentrations of bionanocomposite. The bacterial cells were fixed on glass slides with primary fixative reagents (2.5% glutaraldehde, 0.1 mL paraformaldehyde in sodium cacodylate buffer) and incubated at 4 °C for 1 h. After 1 h incubation, bacterial strains were subjected to centrifugation at 1200 rpm for 5 min. Bacterial cell samples were washed thrice with Millipore water. Different concentrations of ethanol (5%, 15%, 25%, 35%, 45%, 55%, 65%, 80% and 100%) in water were used to dehydrate the bacterial cell samples. These dehydrated samples were dried in oven at 40 °C. A thin layer carbon tape was used to place dried bacterial cells on SEM stub and coated with a sputter (K575-Sputter Coater Emitech, Kent, UK). Finally, the sub-mounted cell samples were examined by SEM at low voltage (JOEL, Ltd, Tokyo, Japan).

2.8. Anticancer activity

2.8.1. MTT cell viability assay

In-vitro cytotoxicity evaluation was performed in human cervical cancer cells (HeLa cells) using MTT (3-(4, 5- dimethylthiazol-2-yl)-2,5-diphenyltetrazole bromide) assay (Al-Qubaisi et al., 2011). Briefly, HeLa cells were seeded in 96 well plates (1×10^4 cells/well) in Dulbecco's Modified Eagle's Medium (DMEM) containing 10% fetal bovine serum and 1% antibiotic antimycotic solution in a humidified incubator at 37 °C with continuous flow of 5% CO_2. Then cell were treated with different concentrations (50, 250, 500, and 1000 μgmL^{-1}) of test sample and incubated at 37 °C for 24 h. After that, freshly prepared MTT (0.5 $mgmL^{-1}$) was added and incubated for 4 h at37 °C. After the exposure period, the MTT containing medium was discarded from the cells and washed with 400 μL of phosphate buffer solution (PBS, pH 7.4). After washing, the obtained crystal was dissolved in 400 μL of dimethyl sulfoxide (DMSO) and mixed thoroughly. Microplate reader was used to measure the cell viability at the absorbance of 570 nm. The percentage of viability was calculated by using the following equation:

$$Cell\,viability(\%) = Abs570nm(sample)/Abs570nm(control) \times 100$$

2.8.2. Lactate dehydrogenase (LDH) cell cytotoxicity assay

The evaluation of cytotoxicity by LDH assay was performed by obeying previously described method with slight modification (Zhang and Wang, 2013). Briefly, 6 well plates was seeded with 2×10^5 HeLa cells per well and incubated at 37 °C for 24 h in a CO_2 humidified incubator until the cells attained confluent growth. After 24 h incubation, the cells were treated with different doses (50, 250, 500, and 1000 μgmL^{-1}) of test samples and positive control (quercetin), followed by 24 h incubation at 37 °C. After the exposure, 100 μL of supernatant from each well was taken and mixed with 2 mL of Tris-EDTA-NADH buffer and incubated for another 30 min at 37 °C. After this, freshly prepared sodium pyruvate (400 μL) was added to the reaction mixture and cell viability was measured at 340 nm after every 15 sec for 3 min.

2.8.3. Acridine Organge/ ethidium bromide (AO/EB) staining

The formation of apoptotic body and nuclear changes in the HeLa cells was monitored under the fluorescence microscope (Pajaniradje et al., 2014). The nanoparticles treated and untreated HeLa cells were harvested and washed with PBS. 20 μL of cell suspension (0.5×10^6 cell mL^{-1}) were stained with 1 μL of AO/EB (1:1) and incubated for 5 min. After incubation, the residual stain was removed from the cells by washing several times with PBS and observed under the fluorescence microscope.

2.8.4. Estimation of ROS generation

DCFH-DA staining was performed to measure the production of ROS in HeLa cells by obeying the previously described method (Jiang and Li, 2014) with little modification. Briefly, the HeLa cells (2×10^4 cell mL^{-1}) were seeded in RPMI 1640 medium containing confocal glass bottom dish and allowed to attach the HeLa cells. After 24 h, PBS was used to wash the cells and the medium was replaced with nanoparticles incorporated medium (IC_{50} concentration) and incubated for 24 h at room temperature. Afterwards, cold PBS was applied to wash the cells again and stained with 50 μm of DCFH-DA. The DCFH-DA treated cells were then incubated at 37 °C

for 30 min. Finally, the incubated cells were washed with PBS and preserved in 1 mL of PBS. Fluorescence microscope was used to assess the ROS production at 488 nm and 530 nm of excitation and emission wavelengths, respectively.

2.8.5. Morphology of cellular nucleus

The morphology of cell nucleus was studied by applying DAPI staining according to the earlier described protocol (Pajaniradje et al., 2014) with slight modifications. Briefly, RPMI 1640 medium containing confocal glass bottom dish was used to grow the HeLa cells and then cells after 24 h cells were washed with PBS. After washing, the HeLa cells were exposed to nanomaterial samples (IC_{50} concentration) for 24 h. After 24 h treatments, the cells were washed again with PBS and fixed in formaldehyde (4%) at room temperature for 4 min. Finally, 300 μL of DAPI (300 nM) solution was put on the cells at ambient temperature for 5 min under dark conditions and washed again with PBS multiple times to get rid of residual dye. The cells were observed at 358 nm excitation and 461 nm emission wavelengths under the fluorescence microscope.

2.8.6. DNA fragmentation assay

The DNA fragmentation was performed by following Baharara et al. method with little modification (Baharara et al., 2015). The bionanocomposite treated cells were collected and washed thrice with PBS at 4 °C. After washing, centrifugation of cells was done at 3500 rpm for 5 min. The pellets suspended with DNA lysis buffer were collected and incubated for 60 min on an ice. After this, 20 μL of RNAse (20 $mgmL^{-1}$) was added to the pellet suspension and incubated at 37 °C for 1 h. Then, this pellet suspension was treated with 20 μL of Proteinase K (20 $mgmL^{-1}$) and centrifuged for 15 min at 10,000 rpm at 4 °C. The supernatant was aspirated and transferred to micro-centrifuge sterile tubes. Finally, the addition of 0.15 M NaCl and ice cold absolute ethanol resulted in precipitation of DNA. The 70% ethanol was used to wash the precipitated DNA and air dried and eventually dissolved in ultrapure water. The spectrophotometer was used to measure the amount of the isolated DNA. The ethidium bromide containing 1.5% of agarose gel was applied for the electrophoresis of DNA of the test sample (100 μgmL^{-1}), control and DNA ladder. The visualization and picturization of gel was performed on gel documentation system.

3. Results

3.1. Identification of chemical constituents of L. Sativum oil by GC–MS

The solvent Soxhlet extraction of *L. sativum* seeds led to the isolation of light yellow colored oil with 72.6% yield. GC–MS analysis was performed to determine the chemical components of oil and 25 different compounds were detected, accounting for 94.6% of the total oil composition. The identified compounds with their retention time (RI) and relative content in the oil are summarized in Table 1. The major effective components found in *L. sativum* oil were monounsaturated and polyunsaturated fatty acids. 7,10-Hexadecadienoic acid (35.82%) and 11-octadecenoic acid (18.32%) was the most abundant fatty acids detected in the oil. Other prominent fatty acid components present were behenic acid (11.95%), stearic acid (6.23%) and 7,10,13-hexadecatrienoic acid (5.65%), with small amounts of 15-tetracosenoic acid, hexadecanoic acid, heneicosanoic acid, 9,12-hexadecadienoic acid, 10-octadecenoic acid, eicosanoic acid, tetracosanoic acid, 9,12-octadecadienoic acid and tetradecanoic acid (Fig. 1, Table 1).

3.2. Physicochemical and morphological characterization of AgNPs and L. Sativum oil/PEG/ Ag-MgO/ bionanocomposite

3.2.1. UV–Visible analysis

UV–Vis absorbance spectra of pre-synthesised AgNPs and bionanocomposite have been displayed in Fig. 2 and Fig. 3. The successful bioreduction preparation of AgNPs by aqueous extract of *L. sativum* seed was indicated by the color change of the reaction mixture from light yellow to dark brown at different time intervals (0–100 sec) under microwave irradiation (Fig. 2). A characteristic surface plasom vibration band between 410 and 450 nm were observed for AgNPs at approximately 30 s during the reaction nucleation and onset of growth. The intensity of the absorption peak increases with the increase in irradiation time, resulting in overlapping of plasmon bands and the formation of more AgNPs with same sizes which might be due to a stabilizing effect of bioactive components present in *L. sativum* seed extract. The peak intensity suggested that *L. sativum* seed extract increased the bioreduction of Ag^{+} with the persistent production of AgNPs upto 100 sec with slight difference in absorption maxima. Thus, the morphology of the nanoparticles is affected by plasmon surface resonance, due to the mutual vibration of electrons of metal nanoparticles in resonance with light wave serving as the basis for measuring adsorption of the material onto the surface of metal nanoparticles (Anandalakshmi et al., 2016). Moreover, the synthesis of nanoparticles by use of microwave provides a rapid, even heating, and eco-friendly approach, offering a uniform nucleation and growth conditions for the nanoparticles within in a short time span unlike the conventional synthesis (Meng et al., 2016).

As shown in Fig. 3, two distinct peaks were observed in the UV–Vis spectrum of *L. sativum* oil/PEG/Ag-MgO/ bionanocomposite. An intense prominent absorption band at 290 nm characteristic of MgO in the lower UV-region alongwith a broad absorption band at 382 nm associated with AgNPs. The obtained result revealed that the incorporation of MgO onto the Ag layer has resulted in a blue shift from 445 nm to 382 nm in the peak of AgNPs. The shift in the UV-peak is attributed to its particle size that depends on nucleation and growth mechanism based on interband transition or the excitation of plasmon resonance, aggregation of Ag-MgO nanoparticle and interaction of organic constituents with silver and magnesium oxide (Cai et al., 2017). This clearly indicates that the optical property of polymeric Ag-MgO bionanocomposite resulted in reduction of particle size. Furthermore, ultrasound exposure affected the size of bionanocomposite due to the cavitational collapse process leading to inter-particle collision and affecting the physicochemical features of the bionanocomposite. It has been also established that the availability and impacts of the secondary metabolites in *L. sativum* seed extract and oil were responsible for the bio-reduction rate leading to the production of bionanocomposite.

3.2.2. FTIR analysis

The functional groups of different phytochemicals present in the *L. sativum* seed extract and oil responsible for the bioreduction and stabilization of AgNPs and polymeric bionanocomposite were identified between 4000 and 500 cm^{-1} regions of FTIR. Fig. 4 displayed a comparative FTIR spectrum of as-prepared AgNPs and bionanocomposite from the aqueous *L. sativum* seed extract and oil, respectively. A prominent band centered at 3434 cm^{-1} were observed in the FTIR spectrum of AgNPs due to the stretching vibrations of hydroxyl (–OH), carboxyl (COOH), amide (–NH) functional groups of various phytochemicals found in the seed extract in the form of alcohols, carboxylic acids, amines or amides, ethers and esters (Anandalakshmi et al., 2016). However, the intensity of these peaks was shifted to a higher and broader frequency range of 3440–3222 cm^{-1} upon binding

Table 1
Chemical components of *L.sativum* oil by GC–MS.

Peak No	Compound	Retention time (Rt)	Area	Area %
1	Methyl palmitate	10.786	8785	0.07
2	Methyl stearate	15.627	88,668	0.05
3	Capric acid methyl ester	16.207	2,588,259	0.21
4	Methyl linoleate	17.158	7821	0.11
5	8-Nonynoic acid, methyl ester	17.890	1,827,628	0.06
6	Behenic acid, methyl ester	18.662	234,224,872	11.95
7	Eicosanoic acid, methyl ester	19.482	2,178,102	1.12
8	9,12-Hexadecadienoic acid, methyl ester	19.989	28,254,212	2.51
9	7,10-Hexadecadienoic acid, methyl ester	20.273	1,041,148,423	35.82
10	7,10,13-Hexadecatrienoic acid, methyl ester	20.587	225,428,643	5.56
11	Stearic acid, methyl ester	20.892	98,167,478	6.23
12	9,12-Octadecadienoic acid, methyl ester	20.990	10,278,217	0.78
13	Tetradecanoic acid, 12-methyl-, methyl ester	21.278	1,675,895	0.72
14	11-Octadecenoic acid, methyl ester	21.982	352,024,326	18.32
15	Hexadecanoic acid, 15-methyl-, methyl ester	22.531	103,093,532	3.54
16	7-Octadecynoic acid, methyl ester	23.423	3,625,642	1.14
17	15-Tetracosenoic acid, methyl ester	23.685	134,871,375	4.56
18	Heneicosanoic acid, methyl ester	24.152	32,721,254	2.15
19	13-Docosenoic acid, methyl ester	24.672	2,531,462	0.65
20	Triacontanoic acid, methyl ester	24.960	2,625,763	0.21
21	10-Octadecenoic acid, methyl ester	25.016	33,219,152	1.25
22	Tetracosanoic acid, methyl ester	25.784	20,624,212	0.96
23	Oleic acid, methyl ester	26.335	2,371,814	0.25
24	Methyl behenate	26.642	94,216	0.11
25	Methyl erucate	27.264	1680	0.07

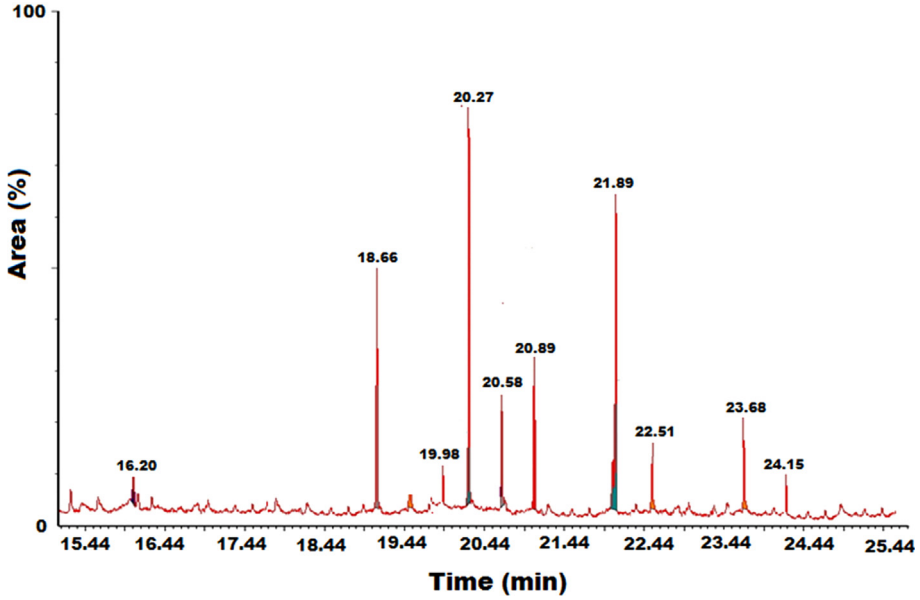

Fig. 1. GC chromatogram of *L. sativum* oil, chemical constituents.

with MgO in *L. sativum* oil/PEG/Ag-MgO/ bionanocomposite. Two sharp peaks at 2898 cm^{-1} and 2787 cm^{-1} were observed in AgNPs which was completely missing in the bionanocomposite spectrum could be assigned to symmetric and asymmetric C-H stretching vibrations of methyl ($-CH_3$), methylene ($-C_2H_2$) and methoxy ($-OCH_3$) groups (Fig. 4b) (Li and Barron, 2010). A vibration band at 1723 $cm^{-1}$was noticed for C-O in AgNPs which was shifted to 1674 cm^{-1} in bionanocomposite, indicating the presence of carboxylate ion and an amide group in the bionanocomposite. Various sharp characteristic peaks between 1525 and 1365 cm^{-1} were observed in both the spectra which were assigned to the asymmetric stretching (C-N), aromatic rings (-C-C-) in addition to the bending vibration of the methyl (–CH3) and methylene groups of fatty acids. The stretching vibration bands at 1238, 1156, and 1032 cm^{-1} were identified for C-O, C-O-C and C-O, respectively. The appearance of absorption band at 568 cm^{-1} wavelength indicates the Mg-O-Mg deformation of the Mg-O (Fig. 4b) (Balamurugan et al., 2014). Thus, the appearance and interaction of the above mentioned bands in *L. sativum* extract and oil clearly suggest that the bioactive constituents serve as reducing and stabilizing agents for the biogenic synthesis of *L. sativum* oil/PEG/Ag-MgO/ bionanocomposite.

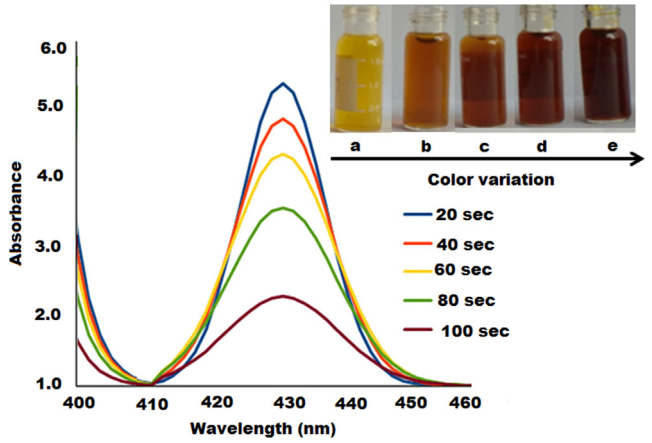

Fig. 2. UV–visible spectra and color variation of biosynthesized silver nanoparticles by using aqueous *L. Sativum* seed extract at the mixing ratio of 2 : 3 different time intervals.

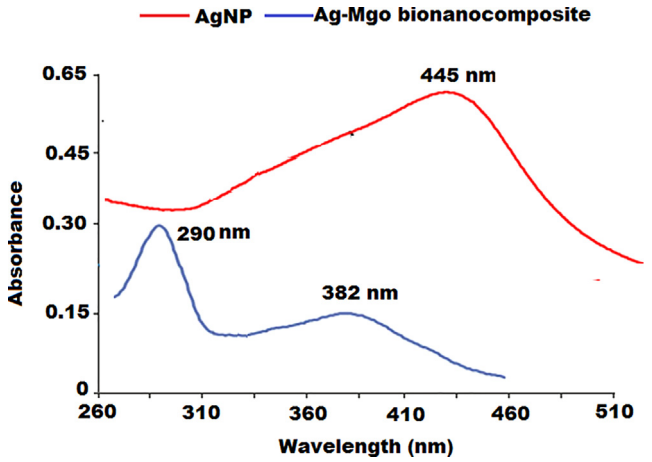

Fig. 3. Comparative UV–vis spectra of AgNPs and *L. sativum* oil/PEG/Ag-MgO bionanocomposite.

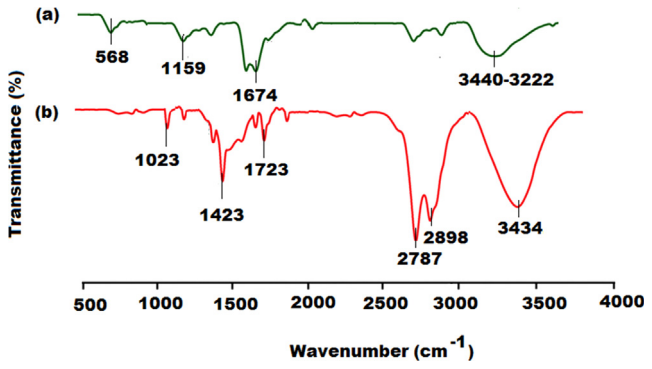

Fig. 4. Comparative FTIR spectra of biosynthesized AgNPs and *L. sativum* oil/PEG/Ag-MgO bionanocomposite.

3.2.3. X-ray diffraction (XRD) analysis

The X-ray diffraction with Cu-Kα radiation (λ = 1540 A) over a range of 20 to 90° was used to confirm the synthesis of AgNPs and dispersion of *L. sativum* oil and Ag-MgO in the PEG polymeric solution of bionanocomposite. The voltage and current applied were 30 kV and 50 mA, respectively. A broad peak appearance for plain PEG in XRD spectrum suggested its amorphous nature

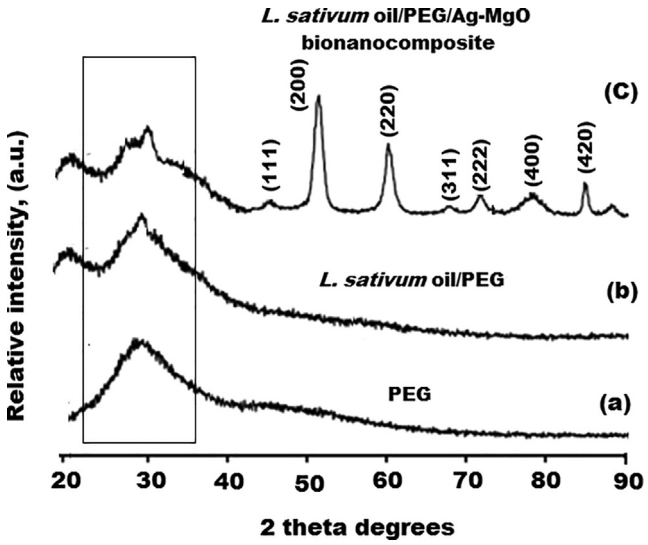

Fig. 5. XRD patterns of (a) plain PEG, (b) *L. sativum* oil/PEG and (c) *L. sativum* oil/PEG /MgO bionanocomposite in the range of 20–90 wavenumber.

(Fig. 5a) (Zhao et al., 2019). However, *L. sativum* oil exhibited a high intensity broad peak near ~30° (Fig. 5a). The XRD pattern revealed that the biosynthesized AgNPs cubical in structure. The bionanocomposite displayed major consistent predominant reflection peaks at 2Θ values ranged between 20 and 90° indexed differently to (111), (200), (220), (311), and (222) allotted to cubical planes of Ag (JCPDS 96–901-2962), alongwith an extended reflection peak at (420) associated with the cubical phase system of MgO (JCPDS 96–901-3264), which has shifted to a higher 2Θ value due to deposited Ag-MgO plane lattice interaction (Fig. 5c). Also, Ag-Mg planer lattice (JCPDS 96–150-9064) was detected, confirming the bionanocomposite nature of the material possessing the cubic crystal lattice network.

3.2.4. Surface morphology

Electron microscopy was used to visualize the morphological and topographical micrograph of biosynthesized AgNPs and polymeric bionanocomposite. Fig. 6a-6 h, showed the surface morphology of PEG, *L. sativum* oil, AgNPs and *L. sativum* oil /PEG/Ag-MgO bionanocomposite. PEG has displayed a smooth face with small diameter at 10000 × and 30000 × magnifications (Fig. 6a and 6b). The images of the plain *L. sativum* oil confirmed that the oil droplets were distorted and homogeneously distributed with irregular edges and small pores on coagulant masses at 10000 × and 30000 × (Fig. 6c and 6d).The SEM images of AgNPs showed uniformly well dispersed spherical nanoparticles (Fig. 6e and 6f), whereas the SEM image of fabricated bionanocomposite image displayed the distribution of Ag-MgONPs in the polymeric matrix with particle size 13.45 nm at the same magnification (Fig. 6g and 6 h). The agglomeration observed in the bionanocomposite may be due the aggregation, polarity, electrostatic attraction and attachment orientation of Ag and MgO nuclei which is clearly presented in Fig. 7. In addition, the presence of high amounts of organic moieties serving as the reducing, capping and stabilizing agents in the *L. sativum* seed extract and oil may also result in the aggregation (Tamilselvi et al., 2013).

Further, the formation of AgNPs and bionanocomposite was substantiated using TEM. Fig. 8 depicts the shape, particle size distribution and morphology of biosynthesized AgNPs and polymeric bionanocomposite through the TEM images. The TEM images of AgNPs and bionanocomposite revealed that the particles were dispersed uniformly and spherical in shape with particle size of

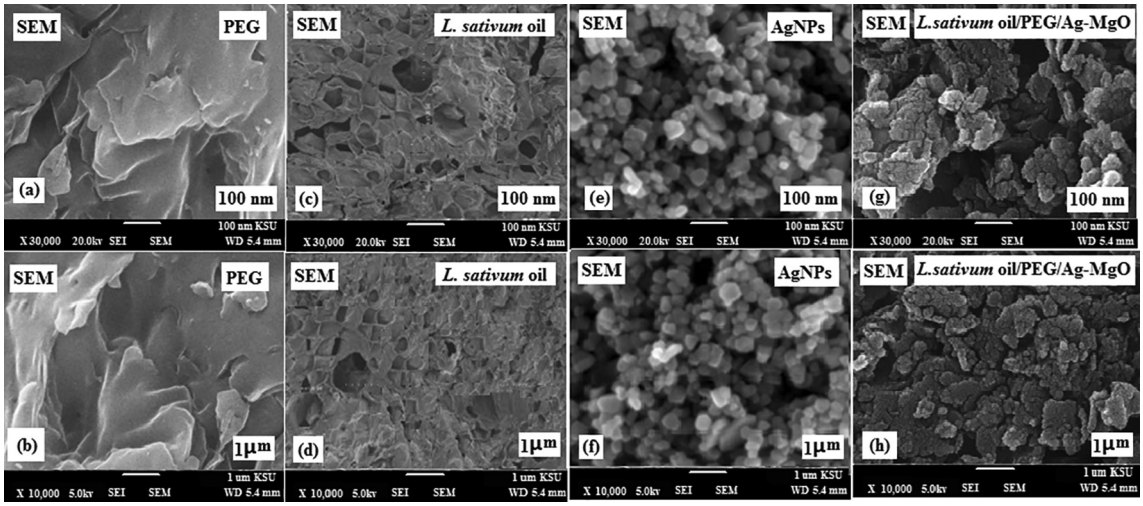

Fig. 6. SEM images of (100 nm and 1 μm): (a and b) plain PEG, (c and d) *L. sativum* oil, (e and f) AgNPs and (g and h) *L. sativum* oil/PEG/Ag-MgO bionanocomposite at different magnifications 10000 × and 30000 ×, magnifications.

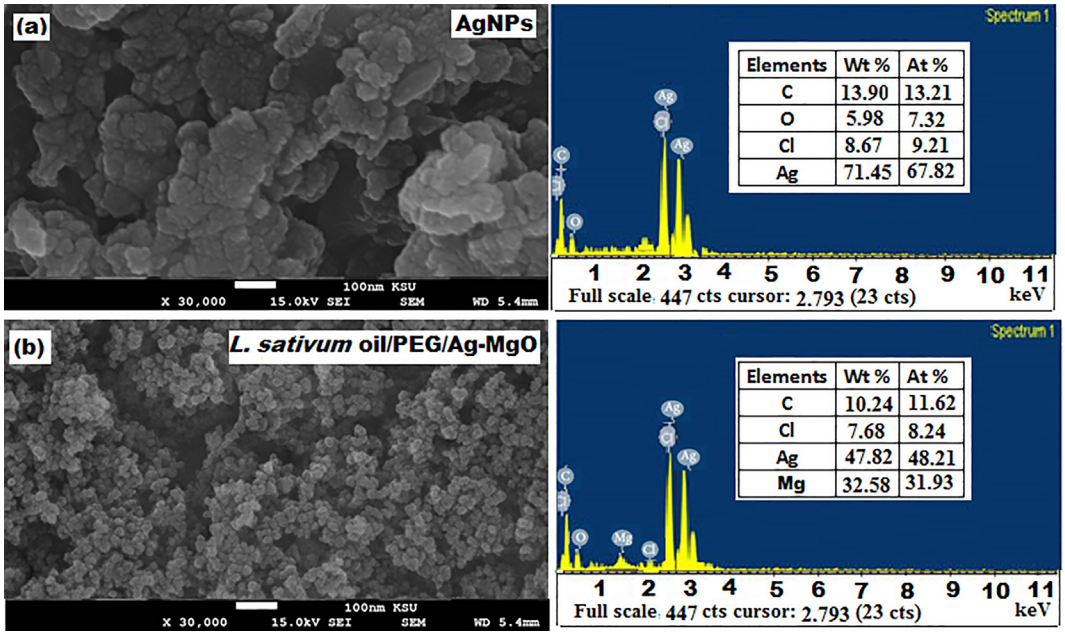

Fig. 7. SEM and EDX images of biosynthesized (a) AgNPs and (b) polymeric bionanocomposite.

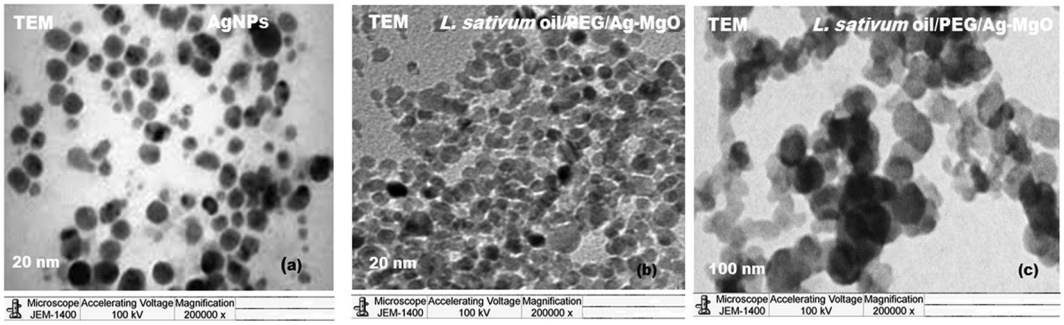

Fig. 8. TEM images of (a) AgNPs; (b) scale bar bionanocomposite image at 20 nm and (c) bionanocomposite image at 100 nm.

16.32 nm and 13.45 nm, respectively (Fig. 8a-c). The distribution and stabilization of the embedded-layered core–shell is due to the interaction between Ag and MgO in the pre-synthesized polymeric bionanocomposite. The soft and smooth surface of the fabricated *L. sativum* oil /PEG/Ag-MgO bionanocomposite can be hypothesized by the appearance of Ag-MgONPs, and revealed the

successful use of *L. sativum* oil with PEG for the preparation of the suggested bionanocomposite. The results showed that the small size and spherical shape of the nanoparticles were well in agreement with the above mentioned shape of the UV–visible plasmon resonance band that the increase in intensity exposure resulted in conversion of larger particle sizes to smaller sizes during the cavitation process.

3.3. Effect of AgNPs and bionanocomposite on the growth inhibition of bacteria

The effect of *L. sativum* oil, AgNPs and pre-synthesised bionanocomposite on the growth of *S. aureus* and *E. coli* was evaluated at different doses by the broth-dilution as well as by plating on agar plates. The appearance of clear zone of inhibition of varying diameters against the test samples with polymeric bionanocomposite showing a wider antibacterial effect on the both bacterial strains. The bionanocomposite displayed a higher level of antibacterial effect on *S. aureus* and *E. coli* with zone of inhibition 27 nm and 24 nm, respectively, in comparison with *L. sativum* oil, and AgNPs (Table 2). The results obtained revealed that increasing concentrations of bionanocomposite had a potential inhibitory effect on the growth of both the bacterial strains (Fig. 9A). The *S. aureus* displayed more prominent bacteriostatic effects as compare to *E. coli*. It was noticed that the treatment of 40 $mgmL^{-1}$ of bionanocomposite inhibited the 80% of *S. aureus* and 75% of *E. coli* growth. However, MIC was observed at 80 $mgmL^{-1}$, the growth of *S. aureus* completely vanished, whereas more than 95% growth of *E. coli* was also inhibited at the similar concentration. The MIC and MBC of the bionanocomposite ranged from 40 to 80 μgmL^{-1} and 80–160 μgmL^{-1}, respectively, against *S. aureus* and *E. coli*. The bactericidal effect of the bionanocomposite might be attributed to many factors. The inactivation mechanism of action of nanomaterials generally towards microorganisms has been a major debate due to the continuous emergence of bacterial resistance (Slavin et al., 2017). However, various studies have suggested that the antibacterial susceptibility and mechanism of nanoparticles, not only depend on the type of bacteria and cell wall structure, but also on the cellular enzymes, contact action and biochemical events involved in production of intercellular reactive oxygen species (ROS) (Ahluwalia et al., 2018; Leung et al., 2014; Zhu et al., 2016). Other responsible factors that may be associated with the death of bacteria could be sizes, surface area and structure of the bionanocomposite. The small sized particle with large surface area possesses strong affinity for interaction, exerting strong bactericidal potential as compared to those larger particles (Raghupathi et al. 2011). Thus, the promising antibacterial activity exhibited by *L. sativum* oil/PEG/Ag-MgO bionanocomposite likely is due the small size and deep penetration of Ag and MgO ions released from *L. sativum* oil/PEG/Ag-MgO bionanocomposite on the adsorbent surface and their interaction with microbial genome and cellular enzymes leading to disruption of the bacterial cell membrane. Furthermore, it has been observed that reducing agents and stabilizers used in preparation of nanomaterials also play decisive roles in determining the antibacterial potential of bionanocomposite (Garmasheva et al., 2016). Thus, the essential oil used in the in the synthesis of *L. sativum* oil/PEG/Ag-MgO bionanocomposite may have contributed to the bactericidal properties due to the presence of different phytochemical components in the *L. sativum* oil (Alqahtani et al., 2019).Table 3.

3.4. Antibacterial activity of bionanocomposite determined by zone of inhibition assay

The biosynthesized bionanocomposite exhibited excellent antibacterial activity towards *S. aureus* and *E. coli*. The zone of inhibition assessments was carried on solid nutrient agar plates. Each agar plate has a well filled with bionanocomposite, which dispersed into the surrounding media and prevented the growth of bacteria in a zone around the well. At 40 mg/well bionanocomposite concentration, an excellent inhibition zone at 27 nm and 24 nm were observerd against *S. aureus* and *E. coli*,respectively (Fig. 9B). The bionanocomposite release and diffuse Ag and MgO ions into the surrounding media, which interact with the inoculated bacteria and significantly stop the bacterial growth around the each well and a clear halo was developed.

3.5. Effect of AgNPs and bionanocomposite on morphology of S. Aureus and E. Coli

The effect of the AgNPs and bionanocomposite on the cellular morphology of *S. aureus* and *E. coli* was explored by SEM. The SEM images of *S. aureus* and *E. coli* showed partial damage and distortion of bacterial cells on treatment with 60 μgmL^{-1} of bionanocomposite (Fig. 10). Images at different magnifications (50,000 to 10,000 ranges) were captured using a 15 kV voltage. Fig. 10a-c and Fig. 10d-f shows cells of *S. aureus* and *E. coli*, respectively. The treatment of AgNPs and bionanocomposite has changed the shape and size of selected bacteria due to nanoparticles coating on the surface bacterial cells. However, the distortion bacterial cells were more pronounced in bionanocomposite treated cells. It was hypothesized that the presence of Ag-Mgo nanoparticles on the surface of bionanocomposite make bacterial cells extremely stressed probably due to an enhanced interaction between bionanocomposite and lipid components of the bacterial cell membrane. This interaction may result in the production of free radical species, which can destroy the transport system of membrane and affect the metabolism and growth of bacterial cell. Previous studies have shown that protoplasmic inclusions and leakage of bacterial cell depends upon the amount of interaction with Ag-MgO naomaterials (Ayinde et al., 2018).

3.6. Anticancer activity of AgNPs and bionanocomposite

The toxicity potential of the synthesized AgNPs and bionanocomposite on human cervical cancer cells was investigated towards HeLa cell line. The cancer cells were exposed to different concentrations of AgNPs and bionanocomposite for 24 h and 48 h. After treatments, the toxicity effects of AgNPs and bionanocomposite was assessed by applying the MTT assay and LDH leakage assay. The MTT results revealed that the AgNPs and bionanocomposite reduced the percentage of cell viability dose and time dependently (Fig. 11A). The inhibitory concentrations (IC_{50}) calculated for AgNPs and polymeric bionanocomposite were

Table 2
Antibacterial activity of *L. stavium* oil, AgNPs and bionanocomposite.

Method	Test samples	MIC (μgmL-1)	Zone of inhibition (mm)	
			S. aureus	*E. coli*
Broth-dilution assay	*L. stavium* oil	120	9.23 ± 0.82	11.65 ± 0.65
	AgNPs	80	18.32 ± 0.56	14.26 ± 0.98
	Bionanocomposite	40	27.01 ± 0.58	24.45 ± 1.16

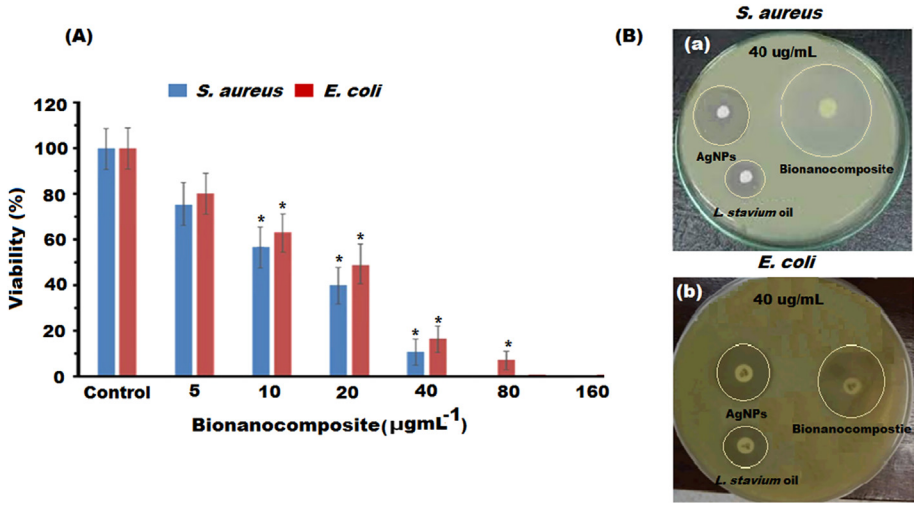

Fig. 9. (A) Effect of bionanocomposite on the growth of *S. aureus* and *E. coli* (B) Zone of inhibition images of (a) *S. aureus* and (b) *E. coli* in the presence of *L. sativum* oil, AgNPs and bionanocomposite.

Table 3
Comparison between the biological activity of the pre-synthesized *L.sativum* oil/PEG/Ag-MgO bionanocomposite film and previously published Ag-MgO based nanocomposites.

Name of nanocomposite	Source	Biological activity	Microorganism and cancer cell lines	Effective concentration μgmL^{-1}	References
Ag-MgO/nanohydroxyapatite (Ag-MgOnHaP)	Ag, MgO, rGO and C. paradisi peel extracts	Antibacterial	*E.coli*, K. pneumonia.	30–60	(Ayinde et al., 2018)
Ag-MgO Nanocomposite	Ag, MgO, and peel extract of *Citrus paradisi*	Antibacterial	E.coli	20–40	(Ayinde et al., 2018)
cauliflower like Ag/MgO nanocomposite	Ag, MgO and cauliflower extract	Antibacterial, anticancer, and catalytic	*E.coli*, *S. aureus*, A549 cancer cells MB, MO, and O-Nip	60 190	(Jayapriya et al., 2019)
L.sativum oil/PEG/Ag-MgO bionanocomposite	Ag, MgO, PEG, And *L.sativum* oil	Antibacterial Anticancer	*S. aureus*, *E. coli* human cervical cancer cells (HeLa)	40 60	Present work

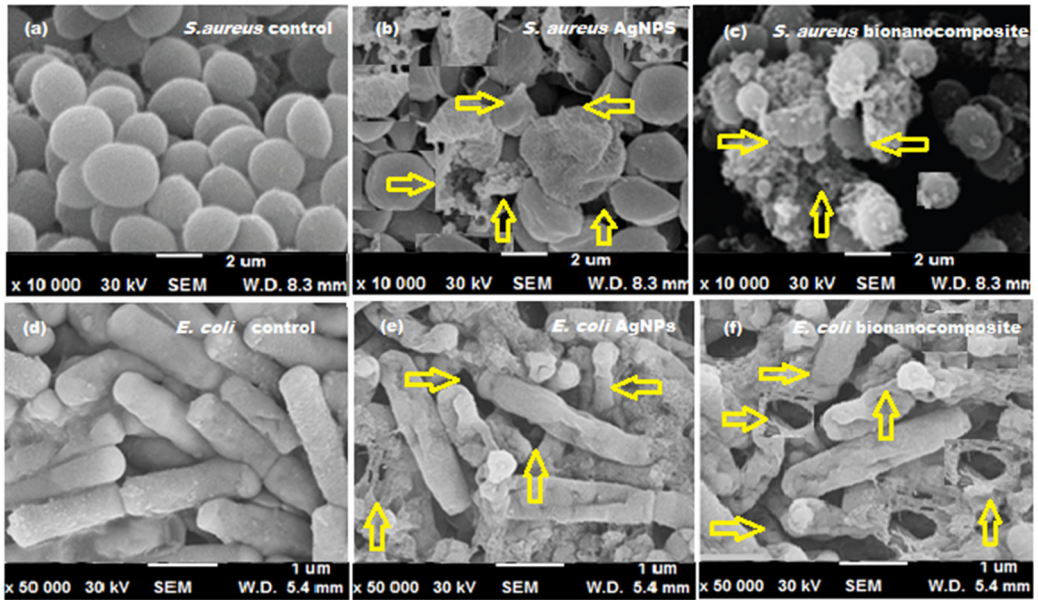

Fig. 10. SEM images of untreated and treated with AgNPs, polymeric bionanocomposite and altered shape of *S. aureus* and *E. coli*.

220.35 μg mL^{-1} and 135 μg mL^{-1}, respectively. The results illustrated the polymeric bionanocomposite induced more cell death than AgNPs due to the presence of magnesium oxide ions which are reported as a cytotoxic agent towards many cancer cell lines including MCF-7, HT 29, Hep2 cells (Amina et al., 2020; Saravanakumar and Wang, 2019). Furthermore, many studies have

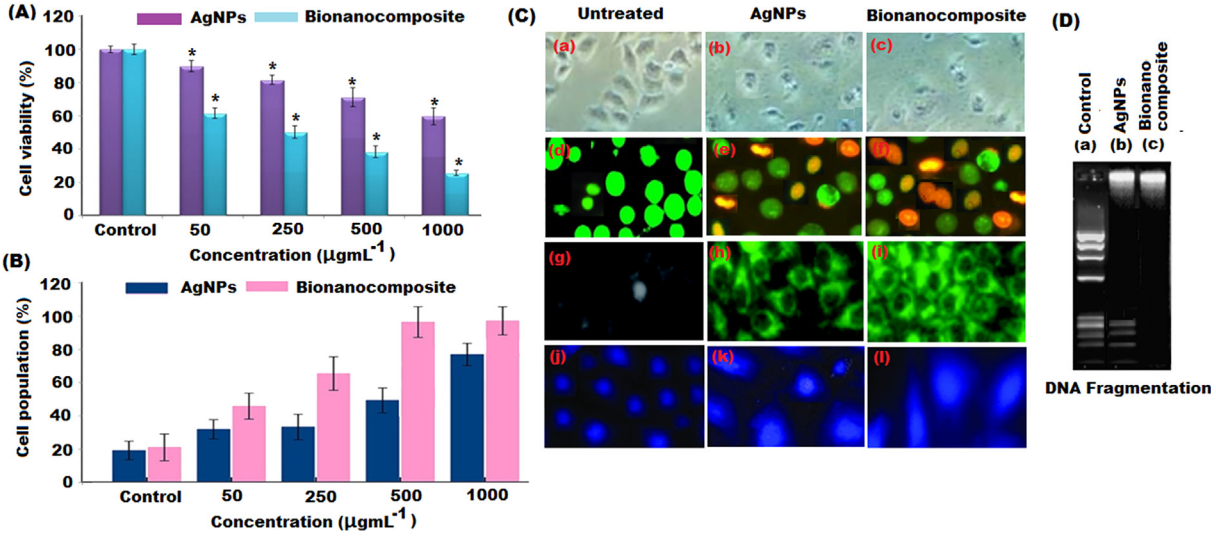

Fig. 11. (A) MTT cell viability assay of biosynthesized AgNPs and bionanocomposite on HeLa cancer cells at 24 h, (B) Apoptosis analysis of AgNPs and bionanocomposite using LHD assay on HeLa cancer cells at 24 h, (C) Effect of AgNPs and bionanocomposite treatments on HeLa cells (a-c) bright field microscopic observation of morphological changes, (d–f) live and dead cells staining by AO/EB,(g–i) ROS generation,(j–l) nucleolus damage by DAPI staining (D) DNA fragmentation in HeLa cells under light microscope.

shown that the silver-doped nanoparticles can easily penetrate the cell membrane and induce the free radicals, production of ROS and trigger the damage of the nucleus (Jayapriya et al., 2020). The morphological changes in the cell and membrane damage were observed under phase contrast microscopic analysis. The obtained results revealed a typical epithelial morphology with high density cell population in the untreated group, whereas chromatin condensation, rounding and shrinkage of cells, membrane blebbing and formation of apoptotic body with less cell population was noticed in AgNPs and bionanocomposite treated cells. These morphological changes might occur due the caspase cascade activation wherein the poly (ADP-ribose) polymerase (PARP) substrate needed for DNA repair mechanism would be cleaved. The cellular absorption of nanoparticles by endocytosis would trigger the production of ROS and actuate the apoptotic pathway and eventually resulting in cell death.

Lactate dehydrogenase (LDH) assay is one of the most commonly applied procedure to examine the cellular or tissue damage based on the level of LDH content in the extracellular medium. LDH is a cytoplasmic soluble enzyme, which is quickly released into the extracellular medium due to cell membrane damage. Thus, the estimation of LDH level is considered as an indicator for the cell toxicity. The cytotoxic effect of the AgNPs and bionanocomposite was further validated by the LDH leakage assay. The results showed that the LDH leakage percentage is concentration dependent in both AgNPS and bionanocomposite treated cells, epitomizing the cell death. However, the bionanocomposite exerted more pronounced cytotoxic effect as compare to AgNPs (Fig. 11B), which could be due to the combined effect of Ag and MgO ions. The aforementioned results were in agreement with the previous report that AgNPs and Ag-MgONPs treatment would permeabilize the cell wall, causing the LDH leakage in lung cancer cells, resulting in cell death (Oh et al., 2014; Saravanakumar and Wang, 2019).

3.6.1. Morphological change observations by using DAPI and acridine orange (AO) staining and bright field microscopy

The fluorescent stains such as DAPI, ethidium bromide (EB) AO label DNA and Hoechst, permit easy visualization of the nucleus in the cells. Herein, the effect of IC_{50} concentrations of these two nanomaterials was analyzed by AO/EB staining, ROS production, followed by nucleus damage by DAPI staining. The AO fluorescent dye can stain both alive and dead cells, but EB dye can stain only dead cells that have lost membrane integrity. However, the AO/EB stains were applied to observe the morphological changes occurred in treated and untreated cells. Whereas, the DAPI staining was performed to monitor the morphological changes induced by AgNPs and bionanocomposite within the nucleus. The DAPI quickly binds to double-stranded DNA groove and the DAPI fluorescence increases 20 fold approximately. For this purpose, HeLa cells were exposed to IC_{50} concentrations of Ag-NPs and polymeric bionanocomposite. The results showed that the treatment of polymeric bionanocomposite induces more apoptosis necrosis (Fig. 11Ca-f), the ROS generation (Fig. 11Cg-i), and the damage of cellular and nuclear membrane (Fig. 11Cj-l) than the AgNPs. The most identified morphological changes noticed in the treated groups were cell shrinkage, cytoplasmic condensation, and nuclear chromatin aggregation. As shown in Fig. 11Bj-l, the AgNPs and bionanocomposite caused morphological alteration and chromatin condensation in the nucleus of HeLa cells, illustrating the fact that the apoptotic effect of AgNPs and bionanocomposite completely dependent on the production of ROS, which in turn has led to the oxidative stress mediated cell death in HeLa cancer cells. After 24 h, the apoptotic cell percentage of Ag-NPs and binocomposite (50, 250, 500 and 1000 μgmL^{-1}) was examined against the HeLa cell line. It is illustrated through the results that with the increase in concentration of nanomaterials, their apoptotic effect significantly increases as well. The bionanocomposite showed 100% apoptotic effect at 500 $\mu gmL\text{-}^{1}$, whereas AgNPs exhibited 86% apoptosis effect on the HeLa cells at 1000 μgmL^{-1} concentrations. The proportion of late late apoptotic (yellow)/necrotic (red) cancer cells significantly increased (1% – 45%), while as the number of live cells dramatically decreased (Fig. 11C). In the DNA fragmentation assay, a fragmented DNA with laddering pattern was noticed in the treated cells, which is considered as an indication of apoptosis. Whereas untreated cells displayed single DNA laddering band (Fig. 11D).

4. Discussion

The biosynthesis of *L. sativum* oil/PEG/Ag-MgO bionanocomposite was eco-friendly and did not require hazardous chemical compounds, high temperatures, or high pressures. The biosynthesized

polymeric bionanocomposite expressed higher antimicrobial effects in comparison with unalloyed AgNPs and pure *L. sativum* oil. A previous study has shown that AgNPs exhibited more toxic effects towards Gram-positive (*S. aureus*) and Gram-negative (*E. coli* and *P. aeruginosa*) bacteria. They concluded that the responsible factor for the toxicity difference of AgNPs was a differentiation in their cell membrane. Also the results confirmed that *E. coli* and *P. aeruginosa* displayed identical sensitivity at equal doses of AgNPs. The enhanced antimicrobial property of biosynthesized bionanocomposite might be due its spherical shape, large surface area, and surface to volume ratio. Additionally, the efficacy of polymeric bionanocomposite increases with the increase in concentration of bionanocomposite. Qais et al (2019) showed that the increasing concentration of silver nanoparticles, the antibacterial properties of nanoparticles towards *S. aureus* and *E.coli* increases. Another study conducted by Ydollahi et al (2016) showed that the antibacterial performance (MIC, MBC) of silver nanoparticles against *S. aureus* and *E.coli* were 100 and 150 μgmL^{-1}, respectively. However, the results of our study showed that the biosynthesized polymeric bionanocomposite and silver nanoparticles exerted antibacterial effects against *S. aureus* at a lower concentration of 40 μgmL^{-1} and 80 μgmL^{-1}, respectively. The higher antibacterial potential of polymeric bionanocomposite is supposedly due to existence of Ag, MgO ions and bioactive constituents, making an advantage compared to the silver nanoparticle. Moreover, the antibacterial action of AgNPs can possibly be attributed to the chemical interaction between lipid bilayer or proteins of bacterial membrane and hydrogen peroxide that induce oxidative stress and damage to proteins and nucleic acids. The AgNPs also penetrate into the cytoplasm and interact with protein and DNA causing cell death. Furthermore, AgNPs can release Ag^{+} ions, causing further damage to the cell. However, the penetration of bionanocomposite into the bacterial cells, release of Ag^{+} and Mg^{2+} ions, increases the intracellular accumulation of nanoparticles, thus destroying the bacterial cells. According to the above results, improvement antibacterial of binonanocomposite is due smaller size of Ag-Mgo with large the surface area and higher concentration of surface defects. SEM and TEM images revealed the spherical shape of nanoparticles, which releases Ag^{+} and Mg^{2+} ions is involved in the bacterial growth inhibition. Our findings suggested that bionanocomposite treated bacterial cells resulted in elevation of ROS generation (Fig. 12 a). The treatment of *S. aureus* with bionanocomposite showed higher production of ROS compared to *E.-coli* that could be explained by the different potentials that are applied to change the surface polarity of Gram-positive and Gram-negative bacteria. The ROS production resulted in bacterial cell membrane disruption, denaturation of protein and other macromolecules damage of bacteria that ultimately leading to cell murder. The toxic effect of biosynthesized polymeric bionanocomposite on HeLa cervical cancer cells starts at 50 μgmL^{-1}, exhibited the more toxic effect than AgNPs biosynthesized by *L. Sativum* seed extract. The bionanocomposite destroyed 100% of HeLa cancer cells at 500 μgmL^{-1} concentrations, whereas ~ 57% of cancerous cells remained alive after treatment with the same concentration of AgNPs. This means that bionanocomposite eliminate cancerous cells twice as higher than AgNPs at similar concentrations. Our results were almost close to earlier findings that reported a 50% decrease in HeLa and MCF-7 cancer cells after treatment with AgNPs at a 27.79 μgmL^{-1} concentration (Abdel-Fattah and Ali, 2018). Bethu et al. (2018) reported that AgNPs in nano-sized dimensions damage the DNA through oxidative stress and lipid peroxidation in human ovarian carcinoma (SKOV3) and human lung adenocarcinoma (A549). They showed that nanostructured substances can be applied as a drug carrier, reducing the non-specific toxicity of strong anticancer agents. Thus nanomaterials with the small size possess unique physiochemical features that provide superior platform of exceptional interaction with proteins, lipids, and nucleic acids present on the surface and within the cell body. Hence, the obtained results revealed that the smaller size of bionanocomposite compared to AgNPs actively triggers apoptotic cell death in HeLa cancer cell line. Moreover, in Ag-Mgo nanoparticles, a part of Mg^{+} ions are substituted by Ag + ions, maintaining the overall neutral charge and oxygen vacancies are created. Also, combination of Ag can make resistance of electron-transfer of MgO decreases, thereby accelerating the electron transfer to the surface to produce $\cdot O_2^-$ by reduction of single electron of adsorbed oxygen on the oxygen vacancy. In brief, the elevation in ROS production and contact interaction between bionanocomposite and cancer cells leads to enhancement of anticancer activity of bionanocomposite (Fig. 12b). Moreover, the presence of different bioactive components of seed oil play an important role in antibacterial and anticancer properties of bionanocomposite. Thus, the excellent antibacterial and anticancer profile of *L. sativum* oil/PEG/Ag-MgO bionanocomposite is the result of synergy between *L. sativum* oil

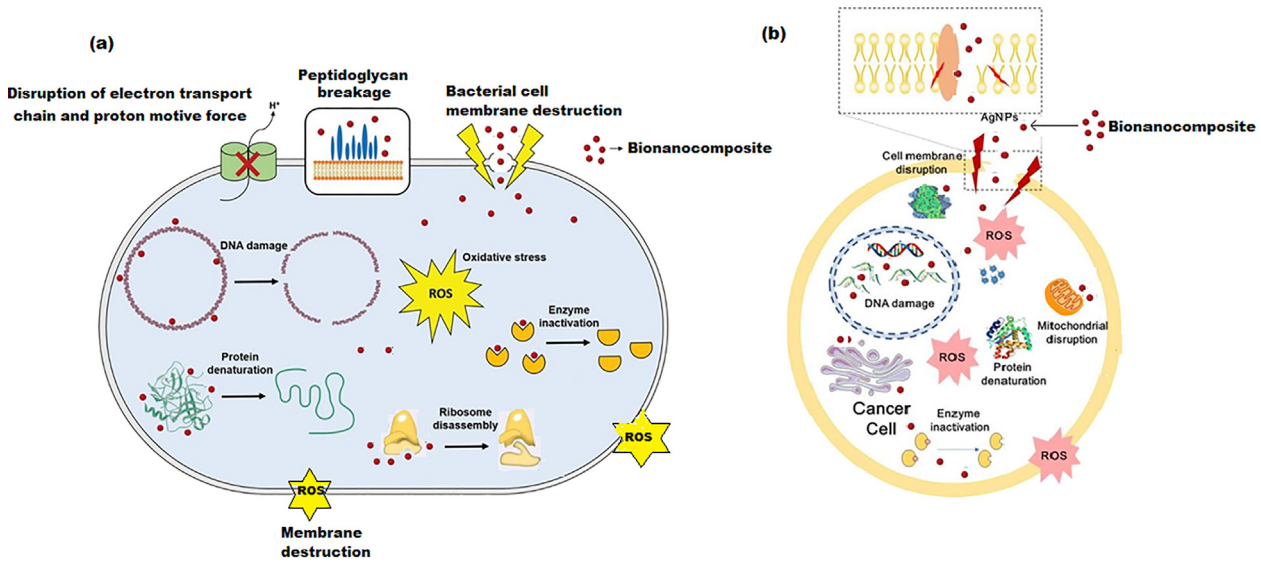

Fig. 12. Schematic (a) antibacterial and (b) anti-cancer mechanisms of bionanocomposite.

components, PEG and Ag-MgO nanoparticles used in its biosynthesis.

The possible mechanism of AgNPs and polymeric bionanocomposite behind the above stated biological properties may be due to free radical species (ROS) that induces oxidative stress which results in the formation of hydroxyl radicals (.OH), superoxide anions (O2.-) and dissolution of cations (Liou and Storz, 2010). Also penetration of these nanoparticles displays cell membrane dissolution that results in inhibition of enzyme activity, DNA synthesis, and upsetting the energy transduction (Podder et al., 2018).

5. Conclusion

The present research work demonstrated the characterization, antibacterial and cytotoxic activity of the biogenic AgNPs *L. sativum* oil/PEG/Ag-MgO bionanocomposite. The high throughput characterization of biomaterial revealed the successful fabrication of polymeric bionanocomposite. Particularly characterization analysis of XRD and TEM results strongly evidenced the formation of a polymeric *L. sativum* oil bionanocomposite enriched with 13.45 nm of silver-magnisium oxide nanoparticles (Ag-MgONPs). The biosynthesized nanomaterials were tested for biological activities including antibacterial and anticancer effects. The outcome of the results showed that both the nanomaterials were sensitive towards the tested *S .aureus* and *E. coli*. However, the bionanocomposite showed strong antibacterial effects against both the strains at a minimum concentration. Furthermore, the anticancer activity against the HeLa cancer cell lines also confirmed that bionanocomposite induced cell death through the enhanced production of ROS followed by cellular and nucleus damage. Conclusively, the results of the study establish that the biogenic synthesis of polymeric bionanocomposite from natural oil, polymer and nanometals leads to the formation pure nanomaterial with antimicrobial and anticancer properties. The bionanocomposite has the potential for the development into promising antibacterial and anticancer drugs for the treatments of multidrug resistance bacteria and cancer.

Data Availability

The data used to support the findings of this study are included within the article.

Declaration of Competing Interest

The authors declare that they have no known competing financial interests or personal relationships that could have appeared to influence the work reported in this paper.

Acknowledgments

The authors extend their appreciation to the Deanship of Scientific Research at King Saud University, for supporting this work through the research group number (RG-1441-540). The authors thank the Deanship of Scientific Research and RSSU at King Saud University for their technical support.

Author's contributions

M.A.: Designed the study; performed the experiment; Draft manuscript. **N.M.A.M.:** Data interpretation. **G.A.A.**: Performed biological study. **A.A.:** Funding Acquisition. **A.E.**: Revise the manuscript; the manuscript. **M.A.A.:** Data compilation. All authors reviewed the manuscript.

Funding

This work was supported by the Deanship of Scientific Research, King Saud University, Research Group.

References

Alam, M., Akram, D., Sharmin, E., Zafar, F., Ahmad, S., 2014. Vegetable oil based eco-friendly coating materials: A review article. Arab. J. Chem. 7 (4), 469–479. https://doi.org/10.1016/j.arabjc.2013.12.023.

Alqahtani, F.Y., Aleanizy, F.S., Mahmoud, A.Z., Farshori, N.N., Alfaraj, R., Al-Sheddi, E. S., Alsarra, I.A., 2019. Chemical composition and antimicrobial, antioxidant, and anti-inflammatory activities of *Lepidium sativum* seed oil. Saudi J. Bio. Sci. 26 (5), 1089–1092. https://doi.org/10.1016/j.sjbs.2018.05.007.

Al-Yahya, M.A., Mossa, J.S., Ageel, A.M., Rafatullah, S., 1994. Pharmacological and safety evaluation studies on *Lepidium sativum* L., Seeds. Phytomedicine 1 (2), 155–159. https://doi.org/10.1016/S0944-7113(11)80035-8.

Abuelgasim, A.I., Nuha, H.S., Mohammed, A.H., 2008. Hepatoprotective effect of *Lepidium sativum* against carbon tetrachloride induced damage in rats. Res. Vet. Sci. 3, 20–23.

Arevalo, F.R., Osorio, S.A., Valcárcel, N.A., Ibarra, J.C., Valero, M.F., 2018. Characterization and in vitro biocompatibility of binary mixtures of chitosan and polyurethanes synthesized from chemically modified castor oil, as materials for medical use. Polym. from Renew. Resour. 9 (1), 23–38. https://doi.org/10.1177/204124791800900102.

Ahmad, J., Bazaka, K., Jacob, M.V., 2014. Optical and surface characterization of radio frequency plasma polymerized 1-isopropyl-4-methyl-1, 4-cyclohexadiene thin films. Electron. 3 (2), 266–281. https://doi.org/10.3390/electronics3020266.

Abudula, T., Qurban, R.O., Bolarinwa, S.O., Mirza, A.A., Pasovic, M., Memic, A., 2020. 3D Printing of Metal/Metal Oxide Incorporated Thermoplastic Nanocomposites With Antimicrobial Properties. Front. Bioeng. Biotechnol. 8. https://doi.org/10.3389/fbioe.2020.568186.

Ayinde, W.B., Gitari, W.M., Munkombwe, M., Amidou, S., 2018. Green synthesis of Ag/MgO nanoparticle modified nanohydroxyapatite and its potential for defluoridation and pathogen removal in groundwater. Phys. Chem. Earth Parts A/B/C. 107, 25–37. https://doi.org/10.1016/j.pce.2018.08.007.

Adams, R. P., 2007. Identification of essential oil components by gas chromatography/mass spectrometry (Vol. 456). Carol Stream, IL: Allured publishing corporation.

Al-Qubaisi, M., Rozita, R., Yeap, S.K., Omar, A.R., Ali, A.M., Alitheen, N.B., 2011. Selective cytotoxicity of goniothalamin against hepatoblastoma HepG2 cells. Molecules 16 (4), 2944–2959. https://doi.org/10.3390/molecules16042944.

Anandalakshmi, K., Venugobal, J., Ramasamy, V., 2016. Characterization of silver nanoparticles by green synthesis method using Pedalium murex leaf extract and their antibacterial activity. Appl. Nanosci. 6 (3), 399–408. https://doi.org/10.1007/s13204-015-0449-z.

Ahluwalia, V., Elumalai, S., Kumar, V., Kumar, S., Sangwan, R.S., 2018. Nano silver particle synthesis using *Swertia paniculata* herbal extract and its antimicrobial activity. Microb. Pathog. 114, 402–408. https://doi.org/10.1016/j.micpath.2017.11.052.

Amina, M., Al Musayeib, N.M., Alarfaj, N.A., El-Tohamy, M.F., Oraby, H.F., Al Hamoud, G.A., Bukhari, S.I., Moubayed, N.M., 2020. Biogenic green synthesis of MgO nanoparticles using Saussurea costus biomasses for a comprehensive detection of their antimicrobial, cytotoxicity against MCF-7 breast cancer cells and photocatalysis potentials. PLoS ONE 15, (8). https://doi.org/10.1371/journal.pone.0237567 e0237567.

Abdel-Fattah, W.I., Ali, G.W., 2018. On the anti-cancer activities of silver nanoparticles. J. Appl. Biotechnol. Bioeng. 5 (1), 43–46. https://doi.org/10.15406/jabb.2018.05.00116.

Burrs, S.L., Vanegas, D.C., Rong, Y., Bhargava, M., Mechulan, N., Hendershot, P., Yamaguchi, H., Gomes, C., McLamore, E.S., 2015. A comparative study of graphene–hydrogel hybrid bionanocomposites for biosensing. Analyst. 140 (6), 2044. https://doi.org/10.1039/c4an01788a.

Bai, L., Bossa, N., Qu, F., Winglee, J., Li, G., Sun, K., Liang, H., Wiesner, M.R., 2017. Comparison of hydrophilicity and mechanical properties of nanocomposite membranes with cellulose nanocrystals and carbon nanotubes. Environ. Sci. Technol. 51 (1), 253–262. https://doi.org/10.1021/acs.est.6b04280.

Bazaka, K., Jacob, M.V., Taguchi, D., Manaka, T., Iwamoto, M., 2011. Investigation of interfacial charging and discharging in double-layer pentacene-based metal-insulator-metal device with polyterpenol blocking layer using electric field induced second harmonic generation. Chem. Phys. Lett. 503 (1–3), 105–111. https://doi.org/10.1016/j.cplett.2010.12.072.

Behzadi, E., Sarsharzadeh, R., Nouri, M., Attar, F., Akhtari, K., Shahpasand, K., Falahati, M., 2019. Albumin binding and anticancer effect of magnesium oxide nanoparticles. Inter. J. Nanomed. 14, 257. https://doi.org/10.2147/IJN.S186428.

Baharara, J., Namvar, F., Ramezani, T., Mousavi, M., Mohamad, R., 2015. Silver nanoparticles biosynthesized using Achillea biebersteinii flower extract: apoptosis induction in MCF-7 cells via caspase activation and regulation of Bax and Bcl-2 gene expression. Molecules 20 (2), 2693–2706. https://doi.org/10.3390/molecules20022693.

Balamurugan, S., Ashna, L., Parthiban, P., 2014. Synthesis of nanocrystalline MgO particles by combustion followed by annealing method using hexamine as a fuel. J. Nanotechnol. 2014. https://doi.org/10.1155/2014/841803.

Bethu, M.S., Netala, V.R., Domdi, L., Tartte, V., Janapala, V.R., 2018. Potential anticancer activity of biogenic silver nanoparticles using leaf extract of Rhynchosia suaveolens: an insight into the mechanism. Artif. Cells Nanomed. Biotechnol. 46 (sup1), 104–114. https://doi.org/10.1080/21691401.2017.1414824.

Climent, M.J., Corma, A., Iborra, S., Mifsud, M., 2007. MgO nanoparticle-based multifunctional catalysts in the cascade reaction allows the green synthesis of anti-inflammatory agents. J. Catal. 247 (2), 223–230. https://doi.org/10.1016/j.jcat.2007.02.003.

Cai, L., Chen, J., Liu, Z., Wang, H., Yang, H., Ding, W., 2018. Magnesium oxide nanoparticles: effective agricultural antibacterial agent against Ralstonia solanacearum. Front. Microbiol. 9, 790. https://doi.org/10.3389/fmicb.2018.00790.

Chiozzi, V., Rossi, F., 2020. Inorganic–organic core/shell nanoparticles: progress and applications. Nanoscale Advances. 2 (11), 5090–5105. https://doi.org/10.1039/D0NA00411A.

Cai, Y., Wu, D., Zhu, X., Wang, W., Tan, F., Chen, J., Qiao, X., Qiu, X., 2017. Sol-gel preparation of Ag-doped MgO nanoparticles with high efficiency for bacterial inactivation. Ceram. Inter. 43 (1), 1066–1072. https://doi.org/10.1016/j.ceramint.2016.10.041.

Diwakar, B.T., Dutta, P.K., Lokesh, B.R., Naidu, K.A., 2010. Physicochemical properties of garden cress (*Lepidium sativum* L.) seed oil. J. Am. Oil Chem. Soc. 87 (5), 539–548. https://doi.org/10.1007/s11746-009-1523-z.

De Conto, D., dos Santos, V., Zattera, A.J., Santana, R.M.C., 2020. Swelling of biodegradable polymers for the production of nanocapsules and films with the incorporation of essential oils. Polym. Bull. 1–18. https://doi.org/10.1007/s00289-020-03465-0.

De Silva, R.T., Mantilaka, M.M., Ratnayake, S.P., Amaratunga, G.A.J., de Silva, K.N., 2017. Nano-MgO reinforced chitosan nanocomposites for high performance packaging applications with improved mechanical, thermal and barrier properties. Carbohydr. Polym. 157, 739–747. https://doi.org/10.1016/j.carbpol.2016.10.038.

George, G., Sisupal, S.B., Tomy, T., Kumaran, A., Vadivelu, P., Suvekbala, V., Sivaram, S., Ragupathy, L., 2018. Facile, environmentally benign and scalable approach to produce pristine few layers graphene suitable for preparing biocompatible polymer nanocomposites. Sci. Rep. 8 (1), 1–14. https://doi.org/10.1038/s41598-018-28560-1.

Gupta, Nikhil, Tomoko, Sano, 2020. Metal and Polymer Matrix Composites. JOM 72, 6. https://doi.org/10.1007/s11837-020-04168-7.

Gomathi, A.C., Rajarathinam, S.X., Sadiq, A.M., Rajeshkumar, S., 2020. Anticancer activity of silver nanoparticles synthesized using aqueous fruit shell extract of *Tamarindus indica* on MCF-7 human breast cancer cell line. J. Drug Deliv. Sci. Technol. 55,. https://doi.org/10.1016/j.jddst.2019.101376 101376.

Garmasheva, I., Kovalenko, N., Voychuk, S., Ostapchuk, A., Livins'ka, O., Oleschenko, L. 2016. Lactobacillus species mediated synthesis of silver nanoparticles and their antibacterial activity against opportunistic pathogens in vitro. Bioimpacts: BIT 6 (4):219–223. http://doi.org/10.15171/bi.2016.29.

Hanisch, C., Ni, N., Kulkarni, A., Zaporojtchenko, V., Strunskus, T., Faupel, F., 2011. Fast electrical response to volatile organic compounds of 2D Au nanoparticle layers embedded into polymers. J. Mater. Sci. 46 (2), 438–445. https://doi.org/10.1007/s10853-010-4887-4.

Hoang Thi, T.T., Pilkington, E.H., Nguyen, D.H., Lee, J.S., Park, K.D., Truong, N.P., 2020. The importance of poly (ethylene glycol) alternatives for overcoming PEG immunogenicity in drug delivery and bioconjugation. Polymers. 12 (2), 298. https://doi.org/10.3390/polym12020298.

Hornak, J., Trnka, P., Kadlec, P., Michal, O., Mentlík, V., Šutta, P., Csányi, G.M., Tamus, Z.Á., 2018. Magnesium oxide nanoparticles: dielectric properties, surface functionalization and improvement of epoxy-based composites insulating properties. Nanomaterials. 8 (6), 381. https://doi.org/10.3390/nano8060381.

Hickey, D.J., Ercan, B., Sun, L., Webster, T.J., 2015. Adding MgO nanoparticles to hydroxyapatite–PLLA nanocomposites for improved bone tissue engineering applications. Acta Biomater. 14, 175–184. https://doi.org/10.1016/j.actbio.2014.12.004.

Ismail, N.A., Razali, M.H., 2020. Bio-nanocomposite IPN for Biomedical Application. In: Interpenetrating Polymer Network: Biomedical Applications. Springer, Singapore, pp. 313–337. https://doi.org/10.1007/978-981-15-0283-5_12.

Imre, B., Pukánszky, B., 2013. Recent advances in bio-based polymers and composites: Preface to the BiPoCo 2012 Special Section. Eur. Polym. J. 49 (6), 1146–1150. https://doi.org/10.1016/j.eurpolymj.2013.04.009.

Jayapriya, M., Arulmozhi, M., Balraj, B., 2018. Optical, biological and catalytic properties of ZnO incorporated MgO nanostructures using Musa paradisiaca bract extract. Ceram. Int. 44, 13152–13160. https://doi.org/10.1016/j.ceramint.2018.04.138.

Jayapriya, M., Dhanasekaran, D., Arulmozhi, M., Nandhakumar, E., Senthilkumar, N., Sureshkumar, K., 2019. Green synthesis of silver nanoparticles using *Piper longum* catkin extract irradiated by sunlight: antibacterial and catalytic activity. Res. Chem. Intermed. 45 (6), 3617–3631. https://doi.org/10.1007/s11164-019-03812-5.

Jayapriya, M., Premkumar, K., Arulmozhi, M., Karthikeyan, K., 2020. One-step biological synthesis of cauliflower-like Ag/MgO nanocomposite with antibacterial, anticancer, and catalytic activity towards anthropogenic pollutants. Res. Chem. Intermed. 46 (3), 1771–1788. https://doi.org/10.1007/s11164-019-04062-1.

Jiang, G.Z., Li, J.C., 2014. Protective effects of ginsenoside Rg1 against colistin sulfate-induced neurotoxicity in PC12 cells. Cell. Mol. Neurobiol. 34 (2), 167–172. https://doi.org/10.1007/s10571-013-9998-4.

Khalid, A., Norello, R., N Abraham, A., Tetienne, J. P., J Karle, T., WC Lui, E., Xia K, A Tran, P., J O'Connor, A., G Mann, B., De Boer, R., 2019. Biocompatible and biodegradable magnesium oxide nanoparticles with in vitro photostable near-infrared emission: Short-term fluorescent markers. Nanomaterials. 9(10), 1360. https://doi.org/10.3390/nano9101360.

Khan, M., Mahmood, A., Alkhathlan, H.Z., 2016. Characterization of leaves and flowers volatile constituents of *Lantana camara* growing in central region of Saudi Arabia. Arab. J. Chem. 9 (6), 764–774. https://doi.org/10.1016/j.arabjc.2015.11.005.

Liu, H., Jian, R., Chen, H., Tian, X., Sun, C., Zhu, J., Yang, Z., Sun, J., Wang, C., 2019. Application of biodegradable and biocompatible nanocomposites in electronics: Current status and future directions. Nanomaterials. 9 (7), 950. https://doi.org/10.3390/nano9070950.

Liong, M., Lu, J., Kovochich, M., Xia, T., Ruehm, S.G., Nel, A.E., Tamanol, F., Zink, J.I., 2008. Multifunctional inorganic nanoparticles for imaging, targeting, and drug delivery. ACS Nano 2 (5), 889–896. https://doi.org/10.1021/nn800072t.

Linstrom, P.J., Mallard, W.G., 2001. The NIST Chemistry WebBook: A chemical data resource on the internet. J. Chem. Eng. Data 46 (5), 1059–1063. https://doi.org/10.1021/je000236i.

Li, J., Barron, A.R., 2010. Fourier transform infrared spectroscopy of metal ligand complexes. OpenStax-CNX module: m 3, 4660.

Leung, Y.H., Ng, A.M., Xu, X., Shen, Z., Gethings, L.A., Wong, M.T., Chan, C.M., Guo, M. Y., Ng, Y.H., Djurišić, A.B., Lee, P.K., 2014. Mechanisms of antibacterial activity of MgO: non-ROS mediated toxicity of MgO nanoparticles towards *Escherichia coli*. Small 10 (6), 1171–1183. https://doi.org/10.1002/smll.201302434.

Liou, G.Y., Storz, P., 2010. Reactive oxygen species in cancer. Free Radic. Res. 44 (5), 479–496. https://doi.org/10.3109/10715761003667554.

Mousa, M.H., Dong, Y., Davies, I.J., 2016. Recent advances in bionanocomposites: preparation, properties, and applications. Int. J. Polym. Mater. Po. 65 (5), 225–254. https://doi.org/10.1080/00914037.2015.1103240.

Mhd Haniffa, M.A.C., Ching, Y.C., Abdullah, L.C., Poh, S.C., Chuah, C.H., 2016. Review of bionanocomposite coating films and their applications. Polymers. 8 (7), 246. https://doi.org/10.3390/polym8070246.

Maghrani, M., Zeggwagh, N.A., Michel, J.B., Eddouks, M., 2005. Antihypertensive effect of *Lepidium sativum* L. in spontaneously hypertensive rats. J. Ethnopharmacol. 100 (1–2), 193–197. https://doi.org/10.1016/j.jep.2005.02.024.

Matharu, R.K., Ciric, L., Edirisinghe, M., 2018. Nanocomposites: Suitable alternatives as antimicrobial agents. Nanotechnol. 29, (28). https://doi.org/10.1088/1361-6528/aabbff 282001.

Moeini-Nodeh, S., Rahimifard, M., Baeeri, M., Abdollahi, M., 2017. Functional improvement in rats' pancreatic islets using magnesium oxide nanoparticles through antiapoptotic and antioxidant pathways. Biol. Trace Elem. Res. 175 (1), 146–155. https://doi.org/10.1007/s12011-016-0754-8.

Moon, G.D., 2020. Yolk–shell nanostructures: Syntheses and applications for lithium-ion battery anodes. Nanomaterials 10 (4), 675. https://doi.org/10.3390/nano10040675.

Meng, L.Y., Wang, B., Ma, M.G., Lin, K.L., 2016. The progress of microwave-assisted hydrothermal method in the synthesis of functional nanomaterials. Mater. Today Chem. 1, 63–83. https://doi.org/10.1016/j.mtchem.2016.11.003.

Nguyen, N.Y.T., Grelling, N., Wetteland, C.L., Rosario, R., Liu, H., 2018. Antimicrobial activities and mechanisms of magnesium oxide nanoparticles (nMgO) against pathogenic bacteria, yeasts, and biofilms. Sci. Rep. 8 (1), 1–23. https://doi.org/10.1038/s41598-018-34567-5.

Navya, P.N., Madhyastha, H., Madhyastha, R., Nakajima, Y., Maruyama, M., Srinivas, S.P., Jain, D., Amin, M.H., Bhargana, S.K., Daima, H.K., 2019. Single step formation of biocompatible bimetallic alloy nanoparticles of gold and silver using isonicotinylhydrazide. Mater. Sci. Eng., C 96, 286–294. https://doi.org/10.1016/j.msec.2018.11.024.

Oh, S.J., Kim, H., Liu, Y., Han, H.K., Kwon, K., Chang, K.H., Park, K., Kim, Y., Shim, K., An, S.S.A., Lee, M.Y., 2014. Incompatibility of silver nanoparticles with lactate dehydrogenase leakage assay for cellular viability test is attributed to protein binding and reactive oxygen species generation. Toxicol. Lett. 225 (3), 422–432. https://doi.org/10.1016/j.toxlet.2014.01.015.

Patwekar, S.L., 2016. Nanobiocomposite: A new approach to drug delivery system. Asian Journal of Pharmaceutics (AJP): Free full text articles from Asian J. Pharm. 10 (04). http://dx.doi.org/10.22377/ajp.v10i04.902.

Patel, U., Kulkarni, M., Undale, V., Bhosale, A., 2009. Evaluation of diuretic activity of aqueous and methanol extracts of *Lepidium sativum* garden cress (Cruciferae) in rats. Trop. J. Pharm. Res. 8 (3). https://doi.org/10.4314/tjpr.v8i3.44536.

Paranjape, A.N., Mehta, A.A., 2006. A study on clinical efficacy of *Lepidium sativum* seeds in treatment of bronchial asthma. Iranian J. Pharmcol Ther. 5, 55–59.

Pazmiño-Durán, E.A., Giusti, M.M., Wrolstad, R.E., Glória, M.B.A., 2001. Anthocyanins from banana bracts (Musa X paradisiaca) as potential food colorants. Food Chem. 73 (3), 327–332. https://doi.org/10.1016/S0308-8146(00)00305-8.

Pajaniradje, S., Mohankumar, K., Pamidimukkala, R., Subramanian, S., Rajagopalan, R., 2014. Antiproliferative and apoptotic effects of *Sesbania grandiflora* leaves in human cancer cells. Biomed Res. Int. 2014. https://doi.org/10.1155/2014/474953.

Podder, S., Chanda, D., Mukhopadhyay, A.K., De, A., Das, B., Samanta, A., Hardy, J.G., Ghosh, C.K., 2018. Effect of morphology and concentration on crossover

between antioxidant and pro-oxidant activity of MgO nanostructures. Inorg. Chem. 57 (20), 12727–12739. https://doi.org/10.1021/acs.inorgchem.8b01938.
Qais, F. A., Shafiq, A., Khan, H. M., Husain, F. M., Khan, R. A., Alenazi, B., Alsalme, A., Ahmad, I. 2019. Antibacterial effect of silver nanoparticles synthesized using Murraya koenigii (L.) against multidrug-resistant pathogens. Bioinorg. Chem. Appl. 2019. https://doi.org/10.1155/2019/4649506.
Ribeiro-Santos, R., Andrade, M., de Melo, N.R., Sanches-Silva, A., 2017. Use of essential oils in active food packaging: Recent advances and future trends. Trends Food Sci. Technol. 61, 132–140. https://doi.org/10.1016/j.tifs.2016.11.021.
Raghavendra, R.H., Akhilender Naidu, K., 2011. Eugenol and n-3 rich garden cress seed oil as modulators of platelet aggregation and eicosanoids in Wistar albino rats. The Open Nutraceuticals J. 4 (1). https://doi.org/10.2174/1876396001104010144.
Reddy, M.C., Murthy, K.R., Srilakshmi, A., Rao, K.S., Pullaiah, T., 2015. Phytosynthesis of eco-friendly silver nanoparticles and biological applications–a novel concept in nanobiotechnology. Afr. J. Biotechnol. 14 (3), 222–247. https://doi.org/10.5897/AJB2013.13299.
Raghupathi, K.R., Koodali, R.T., Manna, A.C., 2011. Size-dependent bacterial growth inhibition and mechanism of antibacterial activity of zinc oxide nanoparticles. Langmuir 27 (7), 4020–4028. https://doi.org/10.1021/la104825u.
Samarth, N.B., Mahanwar, P.A., 2015. Modified vegetable oil based additives as a future polymeric material. Open J. Org. Polym. Mater. 5 (01), 1 http://creativecommons.org/licenses/by/4.0/.
Song, R., Murphy, M., Li, C., Ting, K., Soo, C., Zheng, Z., 2018. Current development of biodegradable polymeric materials for biomedical applications. Drug Des. Devel. Ther. 12, 3117. https://doi.org/10.2147/DDDT.S165440.
Sushma, N.J., Prathyusha, D., Swathi, G., Madhavi, T., Raju, B.D.P., Mallikarjuna, K., Kim, H.S., 2016. Facile approach to synthesize magnesium oxide nanoparticles by using Clitoria ternatea—characterization and in vitro antioxidant studies. Appl. Nanosci. 6 (3), 437–444. https://doi.org/10.1007/s13204-015-0455-1.
Slavin, Y.N., Asnis, J., Häfeli, U.O., Bach, H., 2017. Metal nanoparticles: understanding the mechanisms behind antibacterial activity. J. Nanobiotechnol. 15 (1), 1–20. https://doi.org/10.1186/s12951-017-0308-z.
Saravanakumar, K., Wang, M.H., 2019. Biogenic silver embedded magnesium oxide nanoparticles induce the cytotoxicity in human prostate cancer cells. Adv. Powder Technol. 30 (4), 786–794. https://doi.org/10.1016/j.apt.2019.01.007.
Torabi, M., Kesmati, M., Pourreza, N., Varzi, H.N., Galehdari, H., 2018. Neurobehavioral and biochemical modulation following administration of MgO and ZnO nanoparticles in the presence and absence of acute stress. Life Sci. 203, 72–82. https://doi.org/10.1016/j.lfs.2018.04.023.
Tripathi, N., Pavelyev, V., Islam, S.S., 2017. Synthesis of carbon nanotubes using green plant extract as catalyst: unconventional concept and its realization. Appl. Nanosci. 7 (8), 557–566. https://doi.org/10.1007/s13204-017-0598-3.
Tamilselvi, P., Yelilarasi, A., Hema, M., Anbarasan, R., 2013. Synthesis of hierarchical structured MgO by sol-gel method. Nano Bull. 2, (1) 130106.
Vasile, C., 2018. Polymeric nanocomposites and nanocoatings for food packaging: A review. Mater. 11 (10), 1834. https://doi.org/10.3390/ma11101834.
Wu, S.H., Tseng, C.T., Lin, Y.S., Lin, C.H., Hung, Y., Mou, C.Y., 2011. Catalytic nano-rattle of Au@ hollow silica: towards a poison-resistant nanocatalyst. J. Mater. Chem. 21 (3), 789–794. https://doi.org/10.1039/C0JM02012E.
Zia, M.A., Joyia, F.A., Ahmad, M.S., Saeed, M.M., Zia, K.M., 2020. Bionanocomposites: uses in applied sciences and their benefits. Bionanocomposite, Green Synthesis and Applications, Micro and Nano Technologies., 535–545 https://doi.org/10.1016/B978-0-12-816751-9.00021-0.
Zubair, M., Ullah, A., 2020. Recent advances in protein derived bionanocomposites for food packaging applications. Crit. Rev. Food Sci. Nutr. 60 (3), 406–434. https://doi.org/10.1080/10408398.2018.1534800.
Zhang, S., Yang, Y., Tong, Z., Gao, B., Gao, N., Shen, T., Wan, Y., Yu, Z., Li, L., Ma, X., Guo, Y., 2020. Self-Assembly of Hydrophobic and Self-Healing Bionanocomposite-Coated Controlled-Release Fertilizers. ACS Appl. Mater. Interfaces 12 (24), 27598–27606. https://doi.org/10.1021/acsami.0c06530.
Zhang, S., Wang, Y.T., 2013. NMDA-induced Excitotoxicity and Lactate Dehydrogenase Assay in Primary Cultured Neurons e965 e965 Bio-protocol 3 (21). https://doi.org/10.21769/BioProtoc.965.
Zhao, Y., Zou, M., Liao, H., Du, F., Lei, F., Tan, X., Zhang, J., Huang, Q., Zhou, J., 2019. Crystallization and Temperature Driven Morphological Evolution of Bio-based Polyethylene Glycol-acrylic Rosin Polymer. Polymers. 11 (10), 1684. https://doi.org/10.3390/polym11101684.
Zhu, X., Wu, D., Wang, W., Tan, F., Wong, P.K., Wang, X., Qiu, X., Qiao, X., 2016. Highly effective antibacterial activity and synergistic effect of Ag-MgO nanocomposite against Escherichia coli. J. Alloy. Compd. 684, 282–290. https://doi.org/10.1016/j.jallcom.2016.05.179.
Yadav, Y.C., 2010. Nephroprotactive and curative activity of *Lepidium sativum* seeds in albino rats using cisplatin induced acute renal failure. *Der* Pharma Chem. 2 (4), 57–64.
Ydollahi, M., Ahari, H., Anvar, A.A., 2016. Antibacterial activity of silver-nanoparticles against *Staphylococcus aureus*. Afr. J. Microbiol. Res. 10 (23), 850–855. https://doi.org/10.5897/AJMR2016.7908.